Powder Technology 325 (2018) 316–332

Contents lists available at ScienceDirect

Powder Technology

journal homepage: www.elsevier.com/locate/powtec

Investigation of the vibration sorting of non-spherical particles based on DEM simulation

Ying You [a,1], Malin Liu [b,1], Huaqing Ma [a], Lei Xu [a], Bing Liu [b], Youlin Shao [b], Yaping Tang [b], Yongzhi Zhao [a,*]

[a] Institute of Process Equipment, College of Energy Engineering, Zhejiang University, Hangzhou 310027, China
[b] Institute of Nuclear and New Energy Technology, Tsinghua University, Beijing 100084, China

ARTICLE INFO

Article history:
Received 13 May 2017
Received in revised form 30 August 2017
Accepted 1 November 2017
Available online 6 November 2017

Keywords:
Discrete element method (DEM)
Non-spherical particles
Vibration sorting
Separation
Super-ellipsoids

ABSTRACT

Vibration sorting is a common means in separating non-spherical particles from spherical particles. In this paper, the discrete element method (DEM) is applied to simulate the behavior of spherical particles and non-spherical particles motion on an inclined vibrating plate (IVP), and the influence of different operating parameters on the separation performance of the mixed particles is investigated. In the DEM simulations, both the spherical and non-spherical particles are modeled by super-ellipsoids. The simulation results show that the optimal vibration amplitude and frequency exist for the high separation efficiency of the mixed particles. The separation efficiency can also be enhanced by properly increasing the friction coefficient or decreasing the restitution coefficient between particles and plate. It is easier to separate the non-spherical particles from the spherical particles by diminishing the sphericity of particles. Besides, as long as the inclination angle of the plate is set at appropriate range and the feed rate of the mixed particles is moderate, the non-spherical particles can be separated effectively from the spherical particles. This research could be helpful for the understanding and optimal design of vibration sorting device.

1. Introduction

Shape separation of particles is very important in many industries associated with particulate and powder technology because it has been realized that the quality level of various industrial materials can be improved by moderately standardizing the shape of particles. In many industrial processes, it is required to separate the wanted materials such as spherical particles from the unwanted materials that are ellipsoidal, dumbbells or other irregular shapes. For example, the fuel element of high temperature gas-cooled reactor (HTGR) is made of coated nuclear fuel particles, and the amount of radioactive material in HTGR mainly depends on the failure rate of the coated nuclear fuel particles under irradiation. In the safety analysis of HTGR, it has been validated that the odd-shaped coated particle fabricated in the producing process is the main reason causing the failure rate of fuel particles, thus how to separate the odd-shaped particles from the spherical coated nuclear fuel particles efficiently is an important work for HTGR. It will be of great significance to ensure the safety of the HTGR fuel element if the irregular particles could be separated from spherical particles accurately in the process of producing the coated nuclear fuel particles.

So far, shape sorting of particles can be carried out by various ways. The researchers have tried to separate spherical particles from non-spherical particles by using the inclined rotating disc separators [1–9], the inclined rotary cylinder separators [10–12], or the inclined vibrating plate (IVP) separators [13–17]. In above methods, the IVP separator has many advantages, for example, there is less damage to particles in the process of separation, and the IVP separator is suitable for separating particles with different shapes, especially it can separate the mixtures of particles into two or more groups [15]. Yang et al. [18] had proved that the irregular nuclear fuel particles can be effectively separated from the spherical nuclear fuel particles by using the inclined vibrating table. However, the effects of various operating parameters on separation process are not very clear, which should be studied to enhance the separation efficiency and accuracy in the scale-up of the fuel element fabrication of the HTGR in the next step. Although several investigators have studied the IVP separator by experiment, little effort has been made in studying the separation behavior of particles under different operating conditions of the IVP or different properties of the particles.

The discrete element method (DEM) is an effective tool for studying the motion of granular materials because it can provide information both in the particle scale and the system scale. Hence, we try to investigate the separation behavior of particles on the IVP using DEM simulation in current research. Since the pioneering work of Cundall and Strack [19], DEM models based on spherical particles have been used

* Corresponding author.
E-mail address: yzzhao@zju.edu.cn (Y. Zhao).
[1] These authors contributed equally to this work.

https://doi.org/10.1016/j.powtec.2017.11.002
0032-5910/

extensively to study granular flows [20]. However, non-spherical particles are difficult to handle in discrete element models despite their importance in many situations. So far, several approaches have been developed to model non-spherical particles, including glued spheres [21–26], polyhedral [27,28], and models that explicitly treat various non-spherical shapes such as ellipsoids [29–35], cylinders [36–38], tablets [25,39,40] and cubes [41,42], see Lu et al. [43] for a comprehensive review. In addition to the above approaches, the method based on super-ellipsoid [44–50], is easier to model and can simulate particles with many different non-spherical shapes only by changing several parameters. The resulting computation speed and prediction accuracy are high. So, it is adopted in this paper to investigate the influence of the different operating conditions on the separation process of non-spherical particles based on the DEM simulation.

In this study, various operating conditions, such as the vibration amplitude (including the horizontal vibration amplitude, A_x, and the vertical vibration amplitude, A_z), the vibration frequency, f, the transverse inclination angle of the IVP, β, the sliding friction coefficient, f_s, and the restitution coefficient, e, between particles and plate, the sphericity of particles, Ψ, the feed rate of particles, q, are investigated based on the DEM simulations, in which the super-ellipsoids are applied to model both the spherical and non-spherical nuclear fuel particles, and will be discussed in further detail hereinafter.

2. Mathematical model

2.1. Model of particles

According to Barr [51] the super-ellipsoids can be described by the so-called inside-outside function:

$$f(x,y,z)=\left(\left|\frac{x}{a}\right|^{s_2}+\left|\frac{y}{b}\right|^{s_2}\right)^{\frac{s_1}{s_2}}+\left|\frac{z}{c}\right|^{s_1}-1=0, \tag{1}$$

where a, b and c are the half-lengths of the particle along the particle's principle axes, and s_1 and s_2 (written as $2/\varepsilon_1$ and $2/\varepsilon_2$ in [51]) control the curvature of the particle edges and are called the shape indices in this paper. s_1 determines the shape of the cross section in the y-z and x-z planes, and s_2 relates to the shape in the x-y plane. Fig. 1 shows four super-ellipsoid particles, which are used in this paper, with different shape indices s_1, s_2 and same half-lengths a, b, and c. For $s_1 = s_2 = 2$, the particle is spherical. When s_1 and s_2 are larger than 2, the particle looks more like a cube as s_1 and s_2 increase. Here, we set s_1 and s_2 to be, 2, 3, 5, and 7 to represent particles with different sphericities. Fig. 2 shows the sphericity of particle with different shape indices, it can be clearly seen that the sphericity of particle gradually decreases with the increase of shape indices of particle.

Note that Eq. (1) can only be used to describe the particle when the center of the super-ellipsoid particle coincides with the origin of coordinate and the three major axes of the super-ellipsoid particle coincide with the three coordinate axes, respectively. In the global coordinate system, when the super-ellipsoid particle is at optional position, a local coordinate system must be introduced to describe the particle, in which the super-ellipsoid particle centroid coincides with the origin of coordinate and the coordinate axes coincide with the major axes of the super-ellipsoid particle, respectively. Then Eq. (1) can be performed coordinate transformation using a matrix $\boldsymbol{A}$ to describe the super-ellipsoid particle:

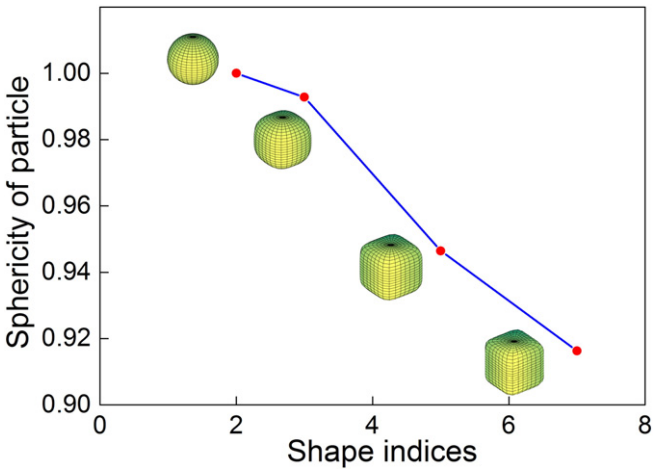

Fig. 2. The sphericity of particle with different shape indices and same half-lengths ($a = b = c$).

$$\begin{pmatrix}\boldsymbol{x}\\1\end{pmatrix}=\begin{pmatrix}\boldsymbol{A}&\boldsymbol{P}\\\boldsymbol{0}&1\end{pmatrix}\begin{pmatrix}\boldsymbol{x}'\\1\end{pmatrix}, \tag{2}$$

$$\boldsymbol{A}=\begin{bmatrix}\cos\psi\cos\varphi-\sin\psi\cos\theta\sin\varphi & -\cos\psi\sin\varphi-\sin\psi\cos\theta\cos\varphi & \sin\psi\sin\theta\\ \sin\psi\cos\varphi+\cos\psi\cos\theta\sin\varphi & -\sin\psi\sin\varphi+\cos\psi\cos\theta\cos\varphi & -\cos\psi\sin\theta\\ \sin\theta\sin\varphi & \sin\theta\cos\varphi & \cos\theta\end{bmatrix}, \tag{3}$$

where $\boldsymbol{x}'=(x',y',z')^T$ is the position vector in the local coordinate system and $\boldsymbol{x}=(x,y,z)^T$ is the position vector global coordinate system, $\boldsymbol{P}=(x_0,y_0,z_0)^T$ is the position vector of the particle centroid in the global coordinate system, $\boldsymbol{0}$ is zero vector, and (ψ, θ, φ) are Euler angles.

2.2. Particle motion equations

The equations of motion for non-spherical particles are the same as those for spherical particles. That is, the translational and rotational movements of a non-spherical particle can be calculated from Newton's second law,

$$m\frac{d\boldsymbol{v}}{dt}=\sum\boldsymbol{F}_c+m\boldsymbol{g}, \tag{4}$$

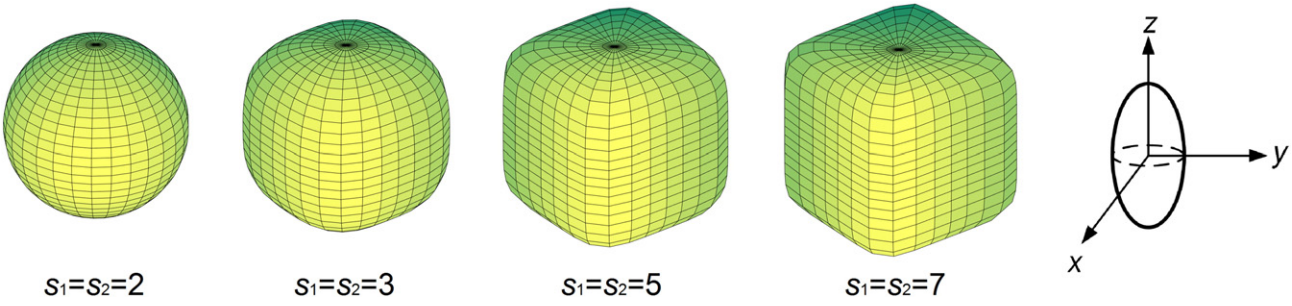

Fig. 1. Spherical and non-spherical particles described by super-ellipsoids ($a = b = c$).

$$\frac{d(\boldsymbol{I}\cdot\boldsymbol{\omega})}{dt}=\sum \boldsymbol{T}_c, \tag{5}$$

where m, $\boldsymbol{v}$, $\boldsymbol{I}$ and $\boldsymbol{\omega}$ are mass, translational velocity, inertia tensor and angular velocity of the individual particle, respectively, $\boldsymbol{g}$ is gravitational acceleration of the particle, $\boldsymbol{F_c}$ is the contact force, and $\boldsymbol{T_c}$ is the contact torque generated by the contact force. Note that the inertia tensor $\boldsymbol{I}$ can be further written as:

$$\boldsymbol{I}=\begin{pmatrix} \int (y^2+z^2)dm & -\int xydm & -\int xzdm \\ -\int yxdm & \int (x^2+z^2)dm & -\int yzdm \\ -\int zxdm & -\int zydm & \int (x^2+y^2)dm \end{pmatrix}, \tag{6}$$

The main difference between spherical particles and non-spherical particles is the rotational motion. For spherical particles the particle orientation is inconsequential, but for non-spherical particles the orientation affects the rotational motion and contact detection. The particle orientation and the rotation matrix can be described by the Euler angles. In order to determine the rotational motion of a non-spherical particle, the moment of inertia of the particle and the contact torques in Eq. (5) must first be calculated. For non-spherical particles, $\boldsymbol{I}$ depends on the coordinate system. In a global coordinate system, $\boldsymbol{I}$ varies with time because of particle rotation. Consequently, a body-fixed coordinate system, also called a local coordinate system, must be used for determining the rotational motion of non-spherical particles [43], then Eq. (5) can be further written as:

$$\left.\begin{aligned} I'_x\frac{d\omega'_x}{dt}+\left(I'_z-I'_y\right)\omega'_y\omega'_z&=T'_{cx}\\ I'_y\frac{d\omega'_y}{dt}+\left(I'_x-I'_z\right)\omega'_z\omega'_x&=T'_{cy}\\ I'_z\frac{d\omega'_z}{dt}+\left(I'_y-I'_x\right)\omega'_x\omega'_y&=T'_{cz}\end{aligned}\right\}, \tag{7}$$

where I_x', I_y' and I_z' are constant, and they are the diagonal elements of the inertial tensor $\boldsymbol{I}'$ in the local coordinate system:

$$\begin{aligned}\boldsymbol{I}'&=\begin{pmatrix} I'_x & 0 & 0\\ 0 & I'_y & 0\\ 0 & 0 & I'_z\end{pmatrix}\\ &=\begin{pmatrix} \int \left(y'^2+z'^2\right)dm & 0 & 0\\ 0 & \int \left(x'^2+z'^2\right)dm & 0\\ 0 & 0 & \int \left(x'^2+y'^2\right)dm\end{pmatrix},\end{aligned} \tag{8}$$

For calculating local angular velocity $\boldsymbol{\omega'}$ in Eq. (7), the contact torque of the particle obtained in the global coordinate system can be firstly converted into the local coordinate system using the inverse matrix $\boldsymbol{A}^{-1}$:

$$\boldsymbol{T}'_c=\boldsymbol{A}^{-1}\boldsymbol{T}_c, \tag{9}$$

The local angular velocity can be obtained by solving the Eqs. (7) and (9). In order to acquire the new angular position of the non-spherical particle in the global coordinate system, the angular velocity obtained in the local coordinate system should be converted into the global coordinate system using the matrix $\boldsymbol{A}$:

$$\boldsymbol{\omega}=\boldsymbol{A}\boldsymbol{\omega}', \tag{10}$$

The new angular velocity $\boldsymbol{\omega}$ obtained in Eq. (10) is used to update the Euler angles. In conclusion, Eqs. (4)–(10) constitute the kinetic equations of a non-spherical particle, and the motion of the non-spherical particle can be determined by solving these kinetic equations.

2.3. Contact model

In DEM simulations, contact detection is a key step of the algorithm. Comparing with spherical particles, the contacts between super-ellipsoids are difficult to calculate. In this paper, the "deepest point method" [43] is employed to detect contact and then determine the overlap of two super-ellipsoid particles. Consider two super-ellipsoid particles $F_1(x,y,z)=0$ and $F_2(x,y,z)=0$ in the global coordinate system, as shown in Fig. 3. If $P_1(x_1,y_1,z_1)$ is any point on the surface of Particle 1, then $F_1(x_1,y_1,z_1)=0$. If $P_1(x_1,y_1,z_1)$ lies inside Particle 2, *i.e.* $P_1(x_1,y_1,z_1)$ meets the condition that $F_2(x_1,y_1,z_1)<0$, then Particle 1 is in contact with Particle 2. On the contrary, if Particle 1 does not contact with Particle 2, there must be a point $P_1(x_1,y_1,z_1)$ meets the condition that $F_2(x_1,y_1,z_1)>0$ and $F_2(x_1,y_1,z_1)$ is the minimum of all $F_2(x,y,z)$. Thus, the problem of calculating the contact detection is transformed into solving the minimum value of the following equations:

$$\text{Objective function}: \ \min F_2(x,y,z) \tag{11}$$

$$\text{Constraint equation}: F_1(x,y,z)=0 \tag{12}$$

In this paper, Lagrange multiplier method is used to solving Eqs. (11) and (12), and the Lagrangian can be written as:

$$L(x,y,z,\lambda)=F_2(x,y,z)+\lambda[F_1(x,y,z)], \tag{13}$$

where λ is the Lagrange multiplier, and L is minimized with respect to the variables x, y, z, and λ.

The Eqs. (11) and (12) can be calculated by taking the derivative of Eq. (13), then the deepest point $P_1(x_1,y_1,z_1)$ on the surface of Particle 1 is found. Repeating above process can find the deepest point $P_2(x_2,y_2,z_2)$ on the surface of Particle 2. If the two super-ellipsoid particles are in contact, a line segment joining the two deepest points represents the overlap $\boldsymbol{\delta}$, and the midpoint of the line segment represents the contact point P_c. For the contact detection between a super-ellipsoid particle and the wall, as shown in Fig. 3b, the overlap is described by the line P_1P_3 rather than the line P_1P_2, the effective contact point is the point P_1 rather than the midpoint of the line P_1P_3, and the action direction is perpendicular to the wall. Except for these mentioned above, the others are same with the contact model between super-ellipsoids.

Once the overlap and the contact point are determined, the contact force and torque along with the subsequent motion of each particle can be calculated similar to traditional DEM for spherical particles [52–55]. The contact force $\boldsymbol{F_c}$ is the sum of the normal contact force $\boldsymbol{F}_{c,n}$ and the tangential contact force $\boldsymbol{F}_{c,t}$:

$$\boldsymbol{F}_c=\boldsymbol{F}_{c,n}+\boldsymbol{F}_{c,t}, \tag{14}$$

In the current model, the contact torque $\boldsymbol{T}_c$ includes the torque $\boldsymbol{T}_t$ generated by the tangential contact force and the torque $\boldsymbol{T}_n$ generated by the normal contact force:

$$\boldsymbol{T}_c=\boldsymbol{T}_t+\boldsymbol{T}_{\mathrm{n}}, \tag{15}$$

The contact forces between two particles can be obtained by using the linear spring-dashpot model which was first proposed by Cundall and Strack [19]. The linear spring-dashpot model estimates the contact force by using a linear spring, a dashpot and a friction slider, where the spring stiffness, the damping coefficients and the coefficients of friction can be obtained from the physical properties of the particles depending on the computational conditions. The normal contact force $\boldsymbol{F}_{c,n}$ and the tangential contact force $\boldsymbol{F}_{c,t}$ in the linear spring-dashpot model are

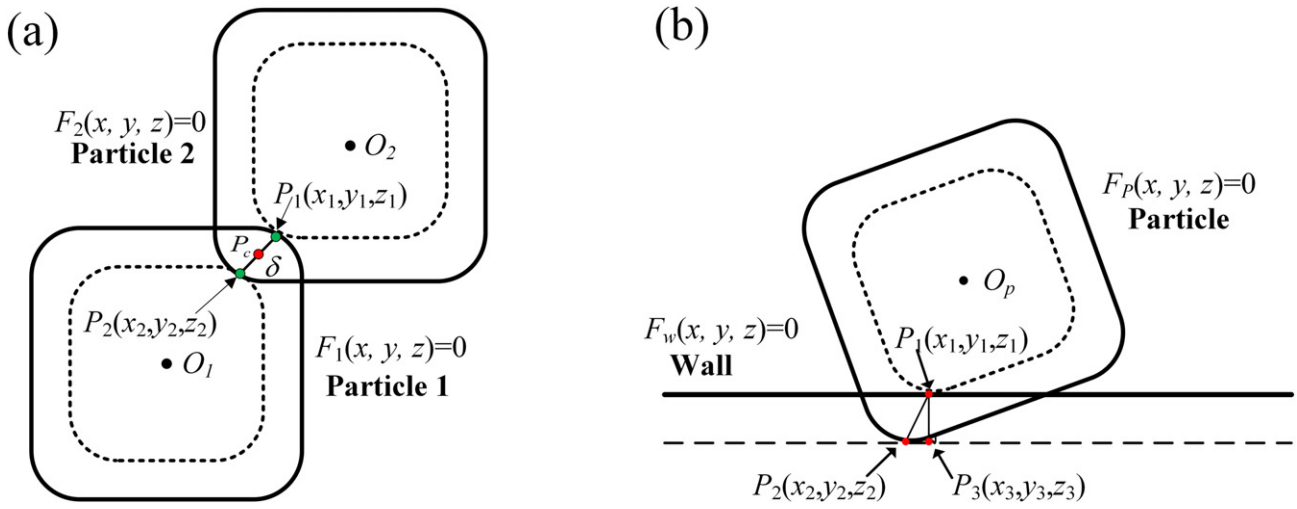

Fig. 3. Contact between (a) two super-ellipsoid particles, (b) super-ellipsoid particle and wall.

given by:

$$\boldsymbol{F}_{c,n} = -k_n\boldsymbol{\delta}_n - \eta_n\boldsymbol{v}_n, \tag{16}$$

$$\boldsymbol{F}_{c,t} = -k_t\boldsymbol{\delta}_t - \eta_t\boldsymbol{v}_t, \tag{17}$$

where $\boldsymbol{\delta}_n$ and $\boldsymbol{\delta}_t$ are the displacements between the particles in the normal direction and tangential direction, respectively, k, η and $\boldsymbol{v}$ are the spring stiffness, damping coefficients and the relative velocities of particles, respectively. The subscripts n and t represent the normal direction and tangential direction, respectively. The damping coefficients can be calculated according to the equations in Ting and Corkum [29] using the restitution coefficients. If the normal contact force $\boldsymbol{F}_{c,n}$ and the tangential contact force $\boldsymbol{F}_{c,t}$ satisfy the following relation:

$$|\boldsymbol{F}_{c,t}| > f_s|\boldsymbol{F}_{c,n}|, \tag{18}$$

then the Coulomb friction model can be used to calculate the tangential contact force $\boldsymbol{F}_{c,t}$, and the equation can be written as follows,

$$\boldsymbol{F}_{c,t} = -f_s|\boldsymbol{F}_{c,n}|\frac{\boldsymbol{\delta}_t}{|\boldsymbol{\delta}_t|}, \tag{19}$$

where f_s is the coefficient of sliding friction.

The torque $\boldsymbol{T}_c$ in Eq. (15) can be calculated by

$$\boldsymbol{T}_c = \boldsymbol{L} \times (\boldsymbol{F}_{c,t} + \boldsymbol{F}_{c,n}), \tag{20}$$

where $\boldsymbol{L}$ is the distance vector from the particle center to the contact point.

2.4. IVP geometrical model

Fig. 4 shows the IVP geometrical model used in separating the non-spherical particles from spherical particles. Fig. 4a is the schematic diagram of the IVP and Fig. 4b is the IVP used in the DEM simulation. The vibrating plate, inclined an angle of β (°) to the horizontal, is subjected to both horizontal vibration (x-driection) and vertical vibration (z-direction) simultaneously. The rectangular coordinate system is established by defining the separator plate as the reference plane, and the mixtures of particles are fed at the origin of the IVP (O) through a feeder, just as shown in Fig. 4a.

The friction imposed on spherical particles on the surface of the IVP is very small, so the spherical particles can easily roll down from the feeder position nearly along the y-direction due to the gravity; on the contrary, the non-spherical particles motion is different from spherical particles. The non-spherical particles mainly slide instead of rolling on the IVP due to their irregular shapes. That is to say, the effect of friction

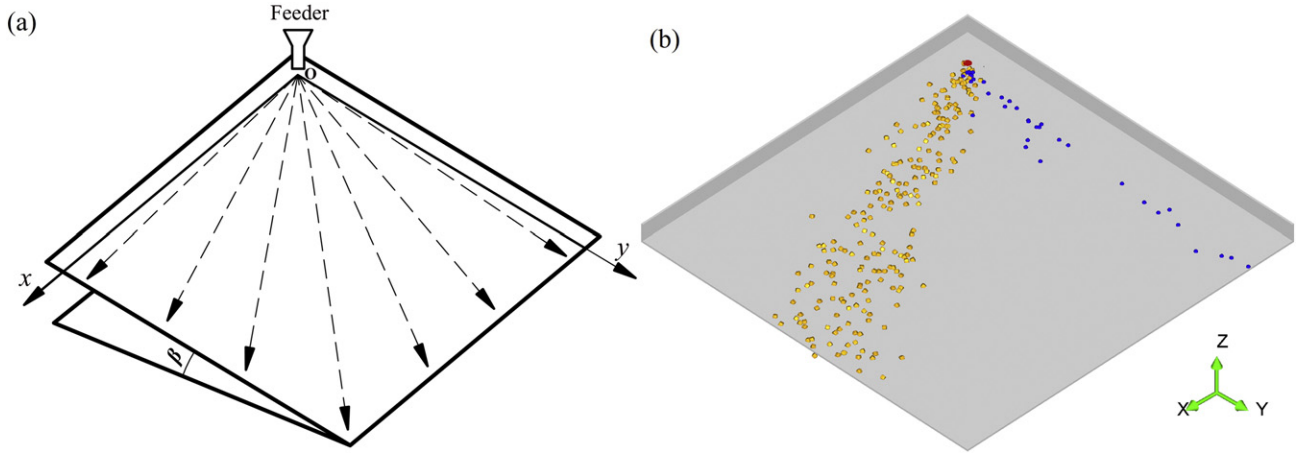

Fig. 4. The IVP geometrical model used in separating the non-spherical particles from spherical particles: (a) the schematic diagram of the IVP and (b) the IVP used in DEM simualtion.

on the non-spherical particles is greater than that of gravity, so they would be transported mainly along the *x*-direction due to the effect of the vibration in this direction, then the non-spherical particles can be separated from the spherical particles, and the movement direction of the two kinds of particles of the bidisperse mixture presents a certain angle, as shown in Fig. 4b. In this study, the influence of air resistance on particle motion is small, so the effect of air resistance on the segregation of particles was ignored. Thus, the average separation angle between spherical particles and non-spherical particles mainly depends on the morphology and mechanical properties of the mixtures, and also the vibrating conditions.

At a moment in the simulation when the separation reaches quasi-static state, the location of each particle on the IVP can be seen as a point. If the point i was connected to the origin of IVP (O), there is an angle (α_i) between the line and the x-axis. The average angle (θ) can be obtained by averaging all angles α_i, which is utilized to describe the overall direction of particles motion on the IVP in this paper. The angle mentioned in the following sections only denotes the average angle (θ) of the spherical particles or the non-spherical particles motion on the IVP, unless otherwise specified. From Fig. 4 it can be clearly seen that the range of the average angle (θ) is from 0° to 90° owing to the structure of IVP, and when particles roll down nearly in the y-direction, the average angle of particles $\theta \approx 90°$; when particles are conveyed nearly in the x-direction, the average angle of particles $\theta \approx 0°$.

2.5. Method of separation evaluation

To describe the separation effect of the mixed particles accurately, the dispersion degree of the spherical particles and non-spherical particles on the IVP are needed to be calculated, respectively. There are two different methods to quantify the dispersion degree of particles, one is the standard deviation (SD) of the angle and the other is the weighted standard deviation (WSD) of the angle. The SD of the angle of particle location can be written as:

$$\sigma = \sqrt{\frac{1}{N}\sum_{i=1}^{N}(\alpha_i - \theta)^2}, \tag{21}$$

and the WSD of the angle of particle location is:

$$\overline{\sigma} = \sqrt{\sum_{i=1}^{N}(\alpha_i - \theta)^2 \frac{L_i}{L}}, \tag{22}$$

where N is the number of particles, $\alpha_i (1 \le i \le N)$ is the angle of each particle location, and the average angle of all particles can be calculated by:

$$\theta = \frac{1}{N}\sum_{i=1}^{N}\alpha_i, \tag{23}$$

If the position of particle i is $A_i = (x, y)$, L_i represents the distance from the location of the particle i to the origin of the IVP (O), which can be expressed as:

$$L_i = \sqrt{x_i^2 + y_i^2} \quad (1 \le i \le N), \tag{24}$$

Then the total distance (L) of all particles can be written as follows:

$$L = \sum_{i=1}^{N}\sqrt{x_i^2 + y_i^2}, \tag{25}$$

It is worthy to note that the WSD used in this study following the rule of weighted distance method and the weighted distance is given by L_i/L.

With the average angle (θ) of particles, the SD and the WSD of the angle of particle locations are utilized to quantify the dispersion degree of particles, and Fig. 5 shows the difference between the SD method and the WSD method. By comparing Fig. 5a with Fig. 5b, it can be seen clearly that adopting the average angle (θ) with the WSD to describe the dispersion degree of particles on the IVP is more accurate than the SD method. The reason is that the nearer the particle position to the origin of the IVP (O), the greater the weight of particles in the SD method. But when we evaluate the separation effect of the mixtures, the weight of the distal particles is more important than the particles fed from the origin of the IVP (O). Therefore, proximal particles weight should be weakened and the remote particle weight should be strengthened, *i.e.*, if we adopt the weight distribution way of "farther is more weight", the calculation results would be more accurate. Thus, the average angle with the WSD is employed in this paper to accurately describe the separation effect of particles.

3. Validation of the DEM model

To validate the DEM model, the comparison between experiment and simulation was performed. Fig. 6 shows the vibration sorting device and particles used in the experiment and the corresponding CAD model of the vibration sorting device, and the particle models used in the DEM simulation. The main components of the vibration sorting device are presented in Fig. 6a: the vibration table, a controller controlling the

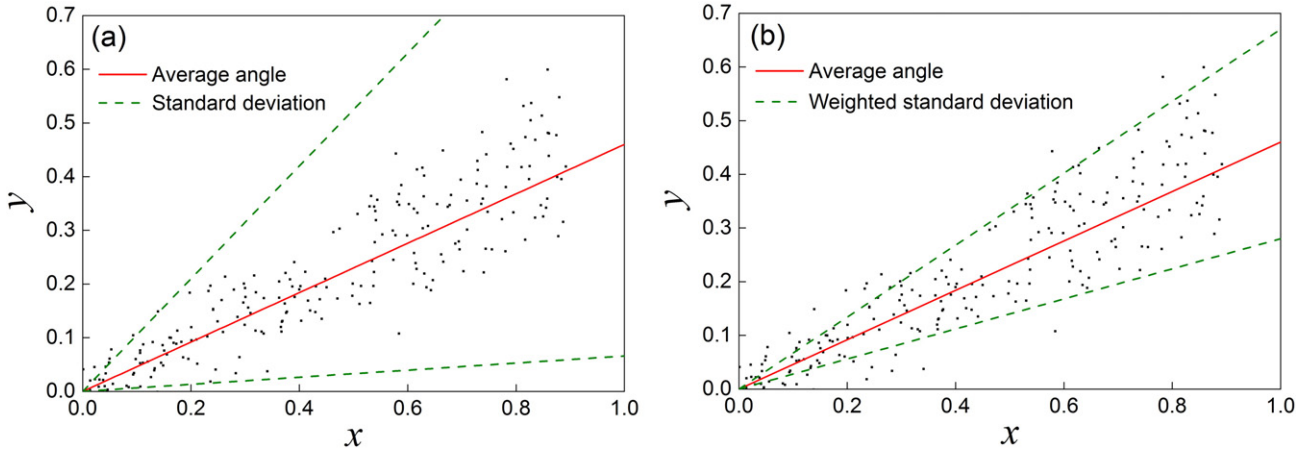

Fig. 5. Comparison between (a) the SD method and (b) the WSD method. Note that the particles shown in the figure are only the non-spherical particles in a simulation case.

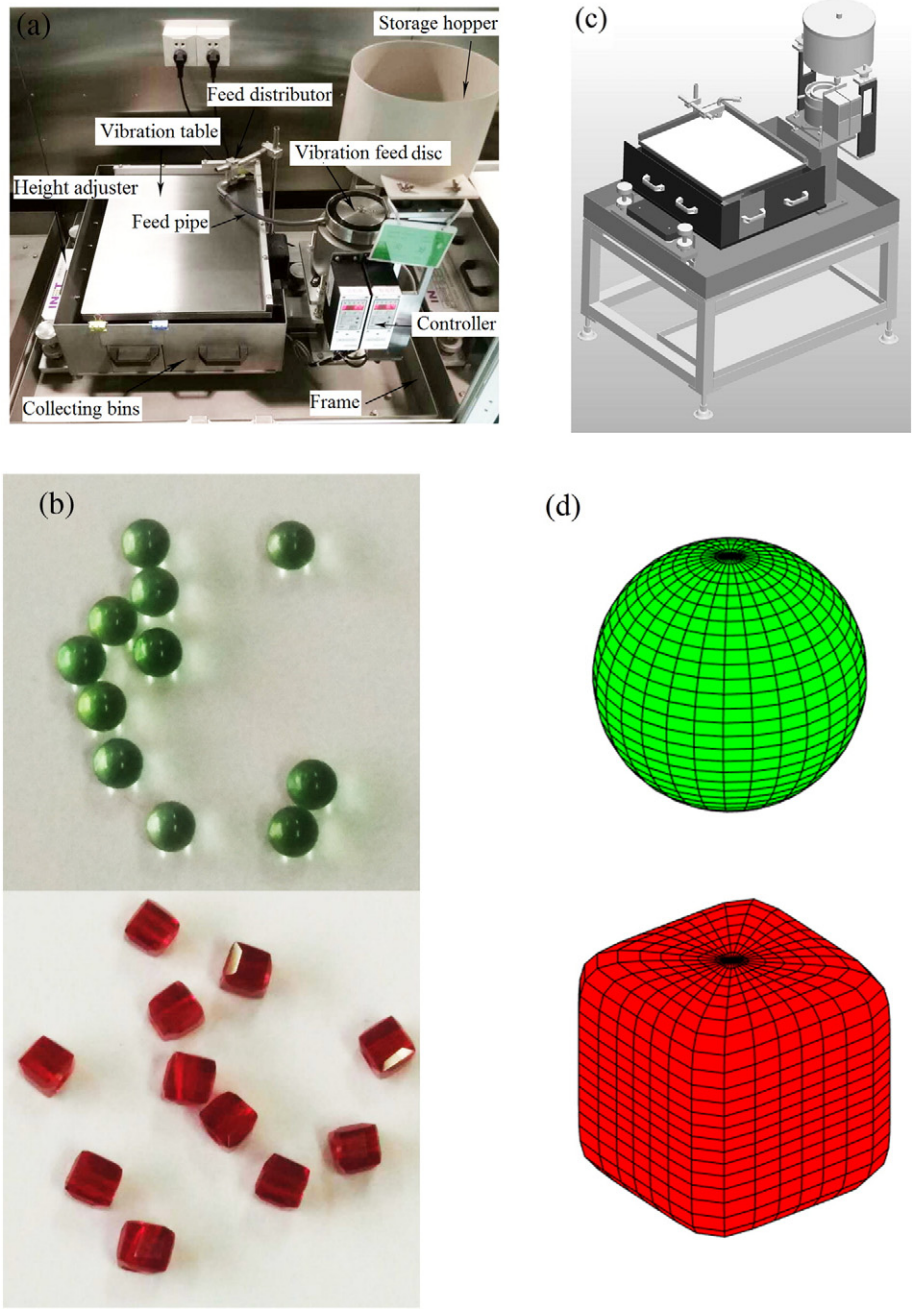

Fig. 6. The vibration sorting device and the particles used in the experiment and the DEM simulation: (a) the laboratory-scale vibration sorting device used in the experiment, (b) particles used in the experiment: sphere (top), non-sphere (bottom), (c) the CAD model of the vibration sorting device, (d) particle models based on super-ellipsoids in DEM simulation: sphere (top), non-sphere (bottom).

vibration amplitude and vibration frequency of the IVP, a height adjuster adjusting the height and inclination angle of the vibrating plate. A storage hopper was used for storing the mixed particles, a vibration feed disc controlling the feed rates of the mixed particles and scattering particles to the vibration table by a feed distributor. Different collecting bins placed underneath the inclined vibrating table were used for collecting the spherical particles and non-spherical particles sorted out from the mixed particles, respectively. The motion of the IVP is simple harmonic vibration, which is induced by a vibrator under the IVP. It should be noted that the actual motion of the IVP is the coupling of the vibration in vertical direction and horizontal direction, which is the same in the DEM simulation.

Fig. 7 shows the snapshots of separation results obtained in the experiment and simulation under the identical operating conditions. Note that the snapshots are obtained when the separation process of the mixtures reaches quasi-steady state. The specific operating parameters in DEM simulations are same as those used in experiments and are listed in Table 1. In order to observe the experimental results conveniently, we used the particles with half-lengths of 1 mm in the model validation section, which is larger than that used in the following sections. From these figures it can be seen clearly that the DEM simulation snapshot matches well with the experiment picture, that is to say, the average angles of the two species on the IVP are basically consistent and the dispersion degree of the spherical particles and non-spherical particles are basically same. From above results it can be found that the inclined vibrating plate based on DEM simulation can be used to simulate the separation process of the mixtures.

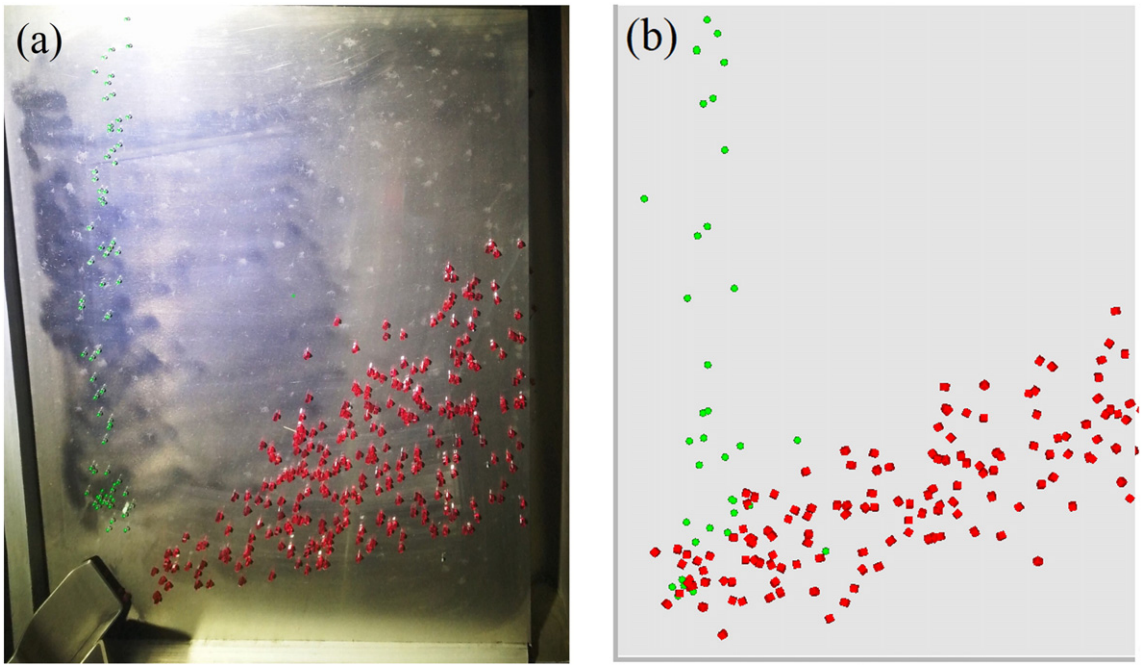

Fig. 7. Comparison of the separation results: (a) experiment and (b) simulation.

4. Simulation conditions

The separation process of the non-spherical particles on the IVP is quite complicated due to the interactions between particles, particles and vibrating plate, the effects of various operating parameters on particles motion, and the quite complicated size distribution of particles. Obviously, it is expensive and difficult to conduct experimental studies on the separation process, especially testing the effects of various operating parameters on separation efficiency of particles by one experimental device. Therefore, adopting DEM simulation in this research can be more convenient and save a lot of costs. In the DEM simulations, all particles are modeled by super-ellipsoids with the half-lengths 0.5 mm, and the number ratio of the spherical particles and the non-spherical particles in the mixtures is 1:1. Note that the size of the vibrating plate in this section is larger than that in the validation tests part above, because the laboratory-scale IVP size is relatively small compared with that in the factory. In what follows, various operating conditions are used in the simulations, the detailed operating parameters adopted in this study are listed in Table 2.

Table 1
Parameters used in experiments and simulations.

Parameters	Experiments	DEM simulations
Parameters of the IVP		
Length (mm)	500	500
Width (mm)	400	400
Inclination angle (°)	3	3
Vibration motion	Harmonic vibration	Harmonic vibration
Parameters of the particles		
Material	Glass	
Shape	Spherical/non-spherical	Spherical/non-spherical
Half-lengths of the particle (mm)	1	1
Density (kg/m^3)	2500	2500
Feed rate (grains/s)	50	50
Mixing ratio	1:1	1:1
Parameters between the particles and the IVP		
Coefficient of friction	0.6	0.6
Coefficient of restitution	0.5	0.5

5. Results and discussion

Numerical studies were performed on the separation process of particles based on the DEM simulations. The DEM simulation data are analyzed in detail from macroscopic and microcosmic perspective. Optimal operating parameters for high separation efficiency were obtained in the present study.

5.1. Effect of the IVP vibration

The vibration amplitude and vibration frequency of the IVP are crucial operation parameters for separating the non-spherical particles from the spherical particles efficiently. The inclined vibrating plate adopted in this study is subjected to both the vertical (z-direction) vibration and horizontal (x-direction) vibration at the same time. For investigating the influence of the vibrating parameters on separation effect, three vibration modes were adopted in this study, respectively,

Table 2
Parameters used in simulations.

Parameters	Value
Parameters of the IVP	
Length (mm)	1000
Width (mm)	1000
Vibration amplitude in x or z direction (mm)	1, 2, 3, 4, 5
Vibration frequency (Hz)	5, 10, 15, 20
Inclination angle (°)	1, 2, 3
Vibration motion	Harmonic vibration
Parameters of the particles	
Material	UO_2
Shape	Spherical/non-spherical
Density (kg/m^3)	3600
Half-lengths of the particle (mm)	0.5
Mixing ratio	1:1
Normal and tangential spring stiffness (N/m)	7000, 2000
Shape indices	3, 5, 7
Particles feed rate (grains/s)	10, 20, 30, 40, 50
Parameters between the particles and the IVP	
Coefficient of friction	0.2, 0.4, 0.6, 0.8
Coefficient of restitution	0.3, 0.6, 0.9

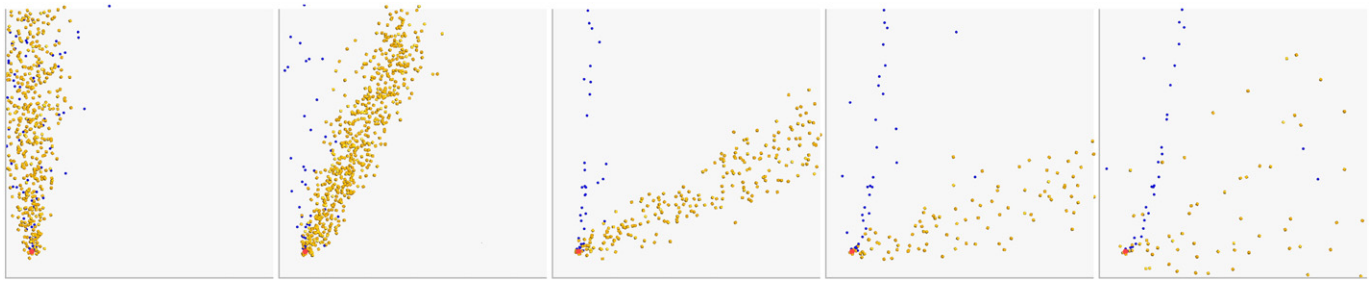

Fig. 8. Snapshots of the spherical particles (blue) and non-spherical particles (yellow) on the IVP, of which the amplitudes in two directions (x- and z-direction), A_x and A_z, are same, are 1, 2, 3, 4, and 5 mm, respectively (from left to right). The other operating conditions are: $\beta = 2°$, $f = 10$ Hz, $f_s = 0.6$, $e = 0.3$, $s_1 = s_2 = 5$, and $q = 30$ grains/s. Note that the snapshots are drawn when the separation of the mixtures reaches quasi-steady state, and the size of particles shown in the figure are ten times bigger than the real ones to ensure that they can be easily seen.

they are given as follows: 1) the horizontal vibration amplitude, A_x, and the vertical vibration amplitude, A_z, of the IVP are same, and are changed simultaneously with the same value and the ranges of the vibration amplitude in both x- and z-directions are varied from 1 mm to 5 mm; 2) the horizontal vibration amplitude, A_x, varying from 1 mm to 5 mm while the vertical vibration amplitude, A_z, is defaulted to a fixed value (3 mm used here); 3) the horizontal vibration amplitude, A_x, is considered as a fixed value (3 mm used here) while researching the effect of the vertical vibration amplitude, A_z, whose range is from 1 mm to 5 mm. For investigating the effect of vibration frequency on separation efficiency, the frequency of the IVP, f, varies from 5 Hz to 20 Hz while the vertical and horizontal vibration amplitudes, A_x and A_z, are defaulted to as a fixed value (3 mm used here).

The simulations of the IVP with the amplitude changing in x- and z-direction at the same time were calculated firstly and the corresponding snapshots are shown in Fig. 8, of which the amplitudes in two directions (x- and z-direction), A_x and A_z, are same and change simultaneously with the same value. Note that the snapshots are drawn when the separation process of the mixtures reaches quasi-steady state. Although the mixing ratio of spherical particles and non-spherical particles is 1:1, from Fig. 8 it can be seen that the number of spherical particles is significantly less than that of non-spherical particles on the IVP when the quasi-steady separation state was attained. The reason is that, the motion of spherical particles on the IVP is mainly rolling while that of the non-spherical particles mainly depends on sliding. The speed of rolling is much faster than sliding on the IVP leading to more spherical particles run out of the table than that of non-spherical particles. Hence, the number of spherical particles is less than non-spherical particles on the IVP when the separation state reaches quasi-steady state. From this figure we also can see that the motion

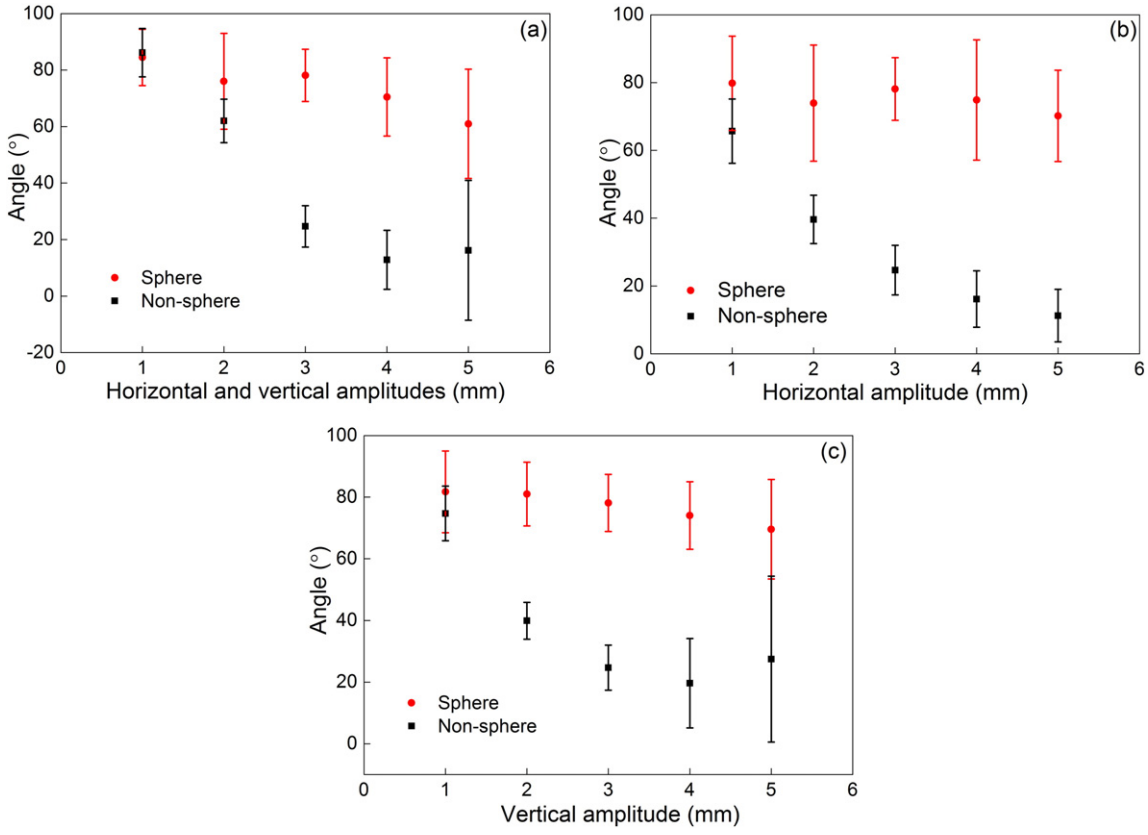

Fig. 9. Effect of the vibration amplitude of the IVP on particle separation efficiency: (a) the vibration amplitudes of two vibration directions (x- and z-direction), A_x and A_z, are same and change simultaneously with the same value; (b) the horizontal vibration amplitudes, A_x, are 1, 2, 3, 4, and 5 mm, respectively, while the vertical vibration amplitude, A_z, is defaulted to a fixed value 3 mm; (c) the vertical vibration amplitudes, A_z, are 1, 2, 3, 4, and 5 mm, respectively, while the horizontal vibration amplitude, A_x, is defaulted to a fixed value 3 mm.The other operating conditions are: $\beta = 2°$, $f = 10$ Hz, $f_s = 0.6$, $e = 0.3$, $s_1 = s_2 = 5$, and $q = 30$ grains/s.

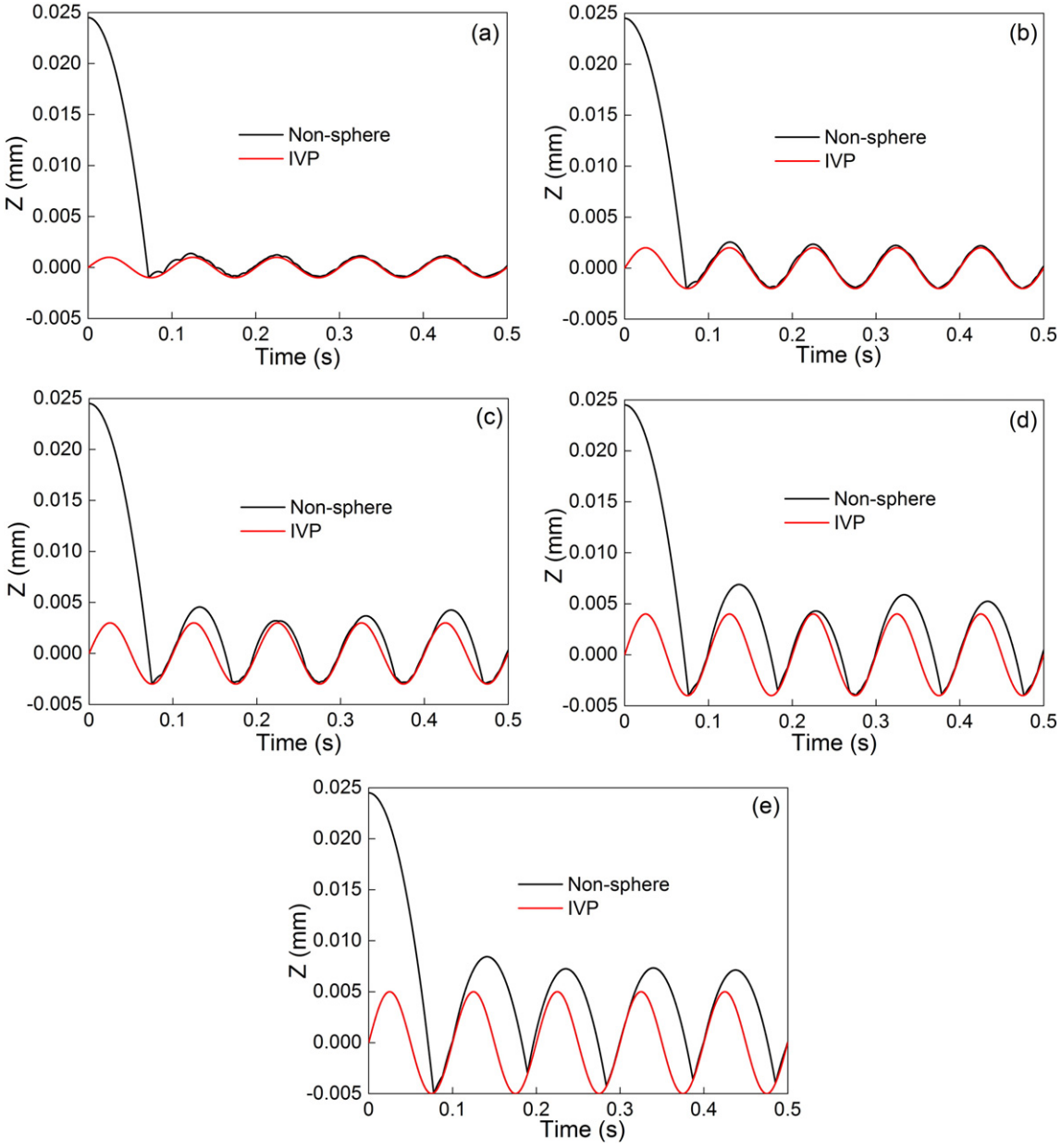

Fig. 10. The z-direction displacement-time curves of a non-spherical particle and the IVP: (a) $A_x = A_z = 1$ mm, (b) $A_x = A_z = 2$ mm, (c) $A_x = A_z = 3$ mm, (d) $A_x = A_z = 4$ mm, (e) $A_x = A_z = 5$ mm. The other operating conditions are: $\beta = 2°$, $f = 10$ Hz, $f_s = 0.6$, $e = 0.3$, $s_1 = s_2 = 5$, and $q = 30$ grains/s.

trajectories of non-spherical particles are more dispersed than spherical particles. The primary reason should be the polygonal shape of the non-spherical particles, which leads to the contact torque direction is more random than that for the spherical particles when particles contact with the plate.

The effect of the vibration amplitude of the IVP on particle separation is analyzed quantitatively and the average angles of the two species particles on the IVP are shown in Fig. 9. Fig. 9a shows the average angles of the two species particles on the IVP as changing A_x and A_z from 1 mm to 5 mm simultaneously. From this figure it can be seen that the separation angle between the two species particles is almost zero when the amplitude is 1 mm, that is to say, the mixtures have not been separated at all but rolled down nearly in the same direction together. The separation angle gradually grows with the vibration amplitude increases and reaches to the maximum value of about 58° when the vibration amplitude is 4 mm. But when the vibration amplitude further increases to 5 mm, the separation angle drops to about 44° and the dispersion degree of the two species particles reaches to the maximum in the current simulation range, and the separation effect just as shown in the rightmost figure in Fig. 8. Fig. 9b shows the quantitative results of the effect of the horizontal vibration amplitude on particle separation. From this figure it can be seen that the separation angle between the two kinds of particles gradually increases from about 14° to about 60° when the horizontal vibration amplitude increases from 1 mm to 5 mm, but the dispersion degree of spherical particles is large when the amplitude varies from 1 mm to 5 mm. Fig. 9c shows the quantitative results of the effect of the vertical vibration amplitude on particle separation. From this figure it can be seen that the separation angle of the two species gradually increases from about 7° to the maximum value of about 54° when the vertical amplitude increases from 1 mm to 3 mm. But when the vertical amplitude is too large (5 mm here), the separation angle drops to about 42° and dispersion degree of the two species reaches to the maximum value. From these results it can be obtained that when the vibration frequency is constant, neither a too large horizontal vibration amplitude nor a too large vertical vibration amplitude has positive effect on improving the separation efficiency, so we

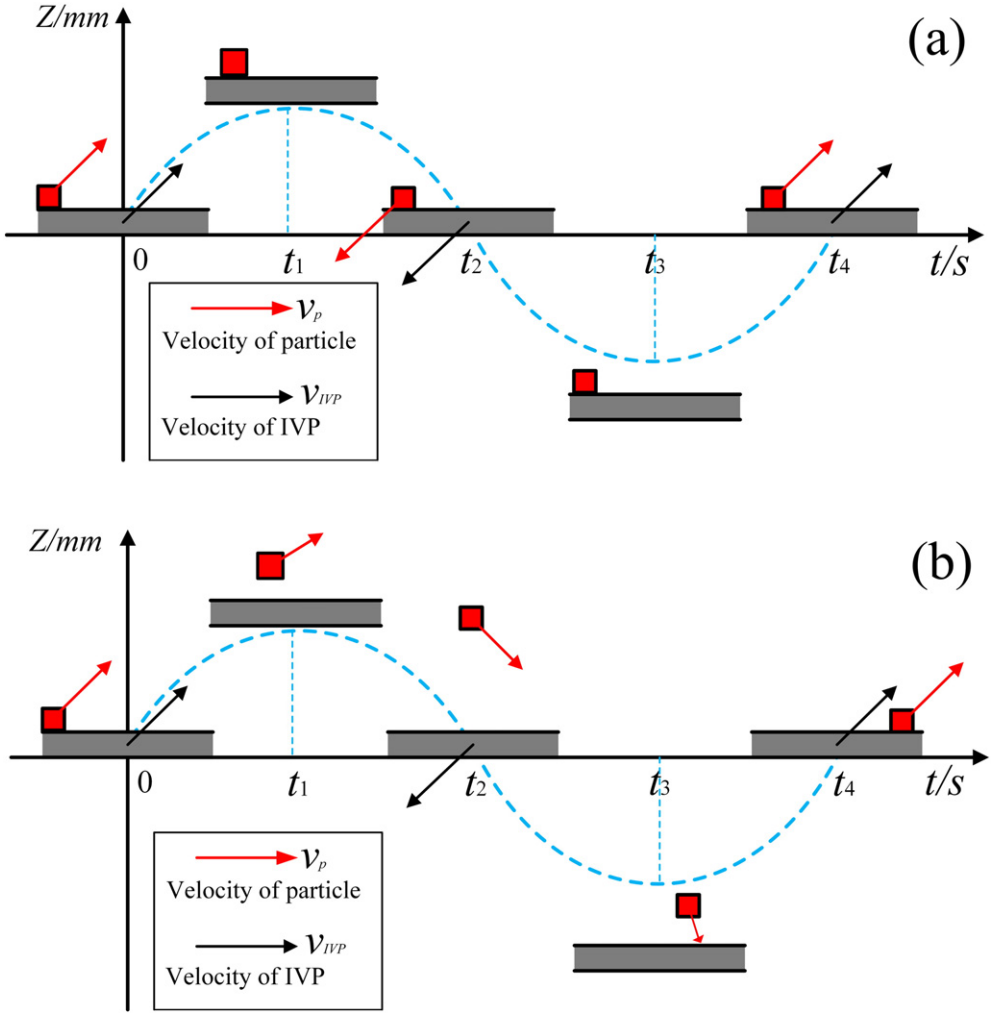

Fig. 11. The z-direction motions of a non-spherical particle and the IVP in one cycle of IVP with harmonic vibration: (a) $A_x = A_z = 1$ mm, (b) $A_x = A_z = 4$ mm.

adopted the first vibration mode mentioned above in all the following simulation cases.

The separation mechanism of the spherical and non-spherical particles on the IVP can be revealed by describing the trajectories of the individual particles. Here, we tracked a non-spherical particle on the IVP. Fig. 10 shows the z-direction displacement-time curves of a non-spherical particle and the IVP under different vibration amplitudes. Fig. 11 shows the schematic diagrams of motions of a non-spherical particle and IVP in one cycle of harmonic vibration. When the amplitude is 1 mm, the non-spherical particle moves with IVP and almost no jumping on the IVP in the whole movement cycle, and the specific motion of the particle and IVP can be described visually by Fig. 11a. With the increase of the amplitude, the particle could bounce from the plate when the IVP moves near the highest location (at around t_1 in Fig. 11b) and keep moving forward when the plate moves down, then the particle falls on the plate when the plate moves to the initial balanced position again (at around t_4 in Fig. 11b). Analyzing the motion of the particle in Figs. 10 and 11, it can be obtained that the particle

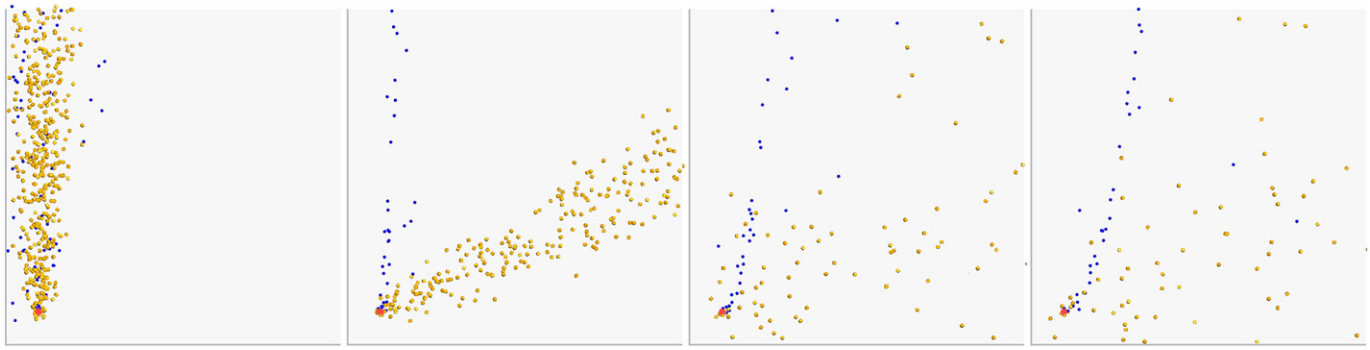

Fig. 12. Snapshots of the spherical particles (blue) and non-spherical particles (yellow) on the IVP, of which the vibration frequencies, f, are 5, 10, 15, and 20 Hz, respectively (from left to right). The other operating conditions are: $\beta = 2°$, $A_x = A_z = 3$ mm, $f_s = 0.6$, $e = 0.3$, $s_1 = s_2 = 5$, and $q = 30$ grains/s. Note that the snapshots are drawn when the separation of the mixtures reaches quasi-steady state, and the size of particles shown in the figure are ten times bigger than the real ones to ensure that they can be easily seen.

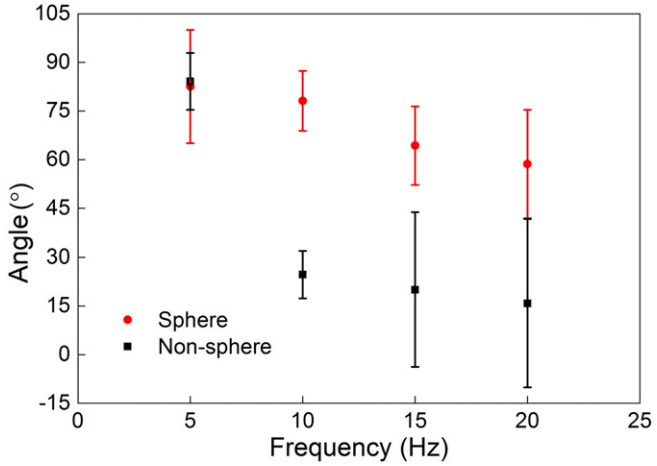

Fig. 13. Effect of the vibrational frequency of the IVP on particle separation. The other operating conditions are: $\beta = 2°$, $A_x = A_z = 3$ mm, $f_s = 0.6$, $e = 0.3$, $s_1 = s_2 = 5$, and $q = 30$ grains/s.

motion in Fig. 10c is most beneficial to separate the non-spherical particle efficiently because the particle could take off from the plate and fall onto the plate at the appropriate time, that is to say, the particle keeps touching with the IVP when the plate moves forward and bounces from the IVP at appropriate height when the plate moves down, so the particle keeps moving forward regularly in the whole cycle. When the vibration amplitude further increases to 5 mm, the residence time of the particle touching with the IVP obviously reduces comparing with the former.

The effect of the vibration frequency of the IVP on sorting is also investigated in this study by changing the frequency of vibrating plate, f, from 5, 10, 15 to 20 Hz, and the corresponding snapshots of the particles on the IVP are shown in Fig. 12. Fig. 13 shows the quantitative results of the effect of the vibration frequency on particle separation. From these figures it can be seen that the vibration frequency of the IVP has a great influence on the particle separation. In the same vibration amplitude (3 mm here), when the vibration frequency is small (5 Hz here), the non-spherical particles cannot be separated from the spherical particles at all and move along the same direction together. When the vibration frequency increases to 10 Hz, the separation of non-spherical particles can be achieved. But when the vibration frequency is >10 Hz, the non-spherical particles are totally scattered on the IVP in disorder. So excessive vibration frequency is not conducive to the separation of non-spherical particles.

The trajectories of a non-spherical particle on the IVP with different vibration frequency are also tracked and analyzed, and the results as shown in Fig. 14. In a cycle of the IVP vibration, when the vibration frequency is 5 Hz, the non-spherical particle moves with IVP together, just like that shown in Fig. 11a. When the vibration frequency increases to 10 Hz, the motion of particle shown in Fig. 14b is similar with the motion shown in Fig. 11b. But when the frequency of the IVP further increases to 15 Hz or 20 Hz, the particle mostly bounce on the IVP and the height of the particle bouncing from the IVP increased dramatically, which lead to the residence time of particle touching with the IVP significantly reduces.

From the above, we can obtain that when the vibration amplitude or frequency of the plate is too small or too large, the non-spherical particles cannot be separated from spherical particles at all. If the particles could take off from the plate at the proper time and could fall back on the plate at the proper time after a period of free fly, the non-spherical particles can be separated from the spherical particles effectively. Thus, it is necessary to find out the critical amplitude and frequency for particle to take off. As mentioned above, the vibration mode of the IVP is simple harmonic vibration, the displacement-time formula and the vibration acceleration formula of the IVP can be written as:

$$y = A \cdot \sin 2\pi f t, \tag{26}$$

$$a = -A \cdot (2\pi f)^2 \sin 2\pi f t, \tag{27}$$

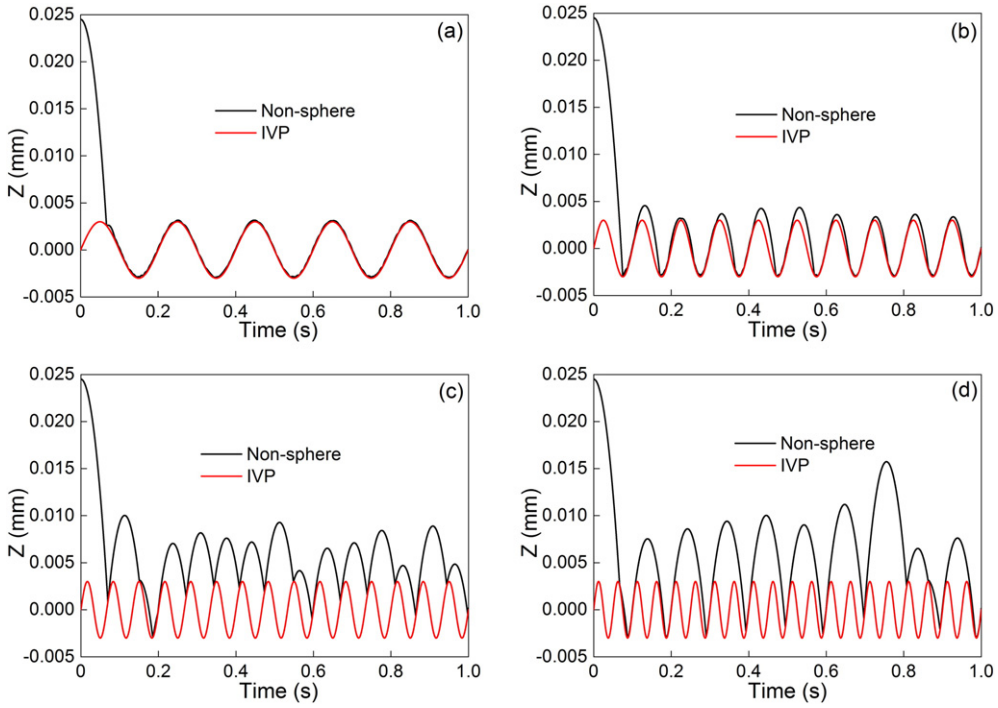

Fig. 14. The z-direction displacement-time curves of the non-spherical particle and the IVP: (a) $f = 5$ Hz, (b) $f = 10$ Hz, (c) $f = 15$ Hz, (d) $f = 20$ Hz. The other operating conditions are: $\beta = 2°$, $A_x = A_z = 3$ mm, $f_s = 0.6$, $e = 0.3$, $s_1 = s_2 = 5$, and $q = 30$ grains/s.

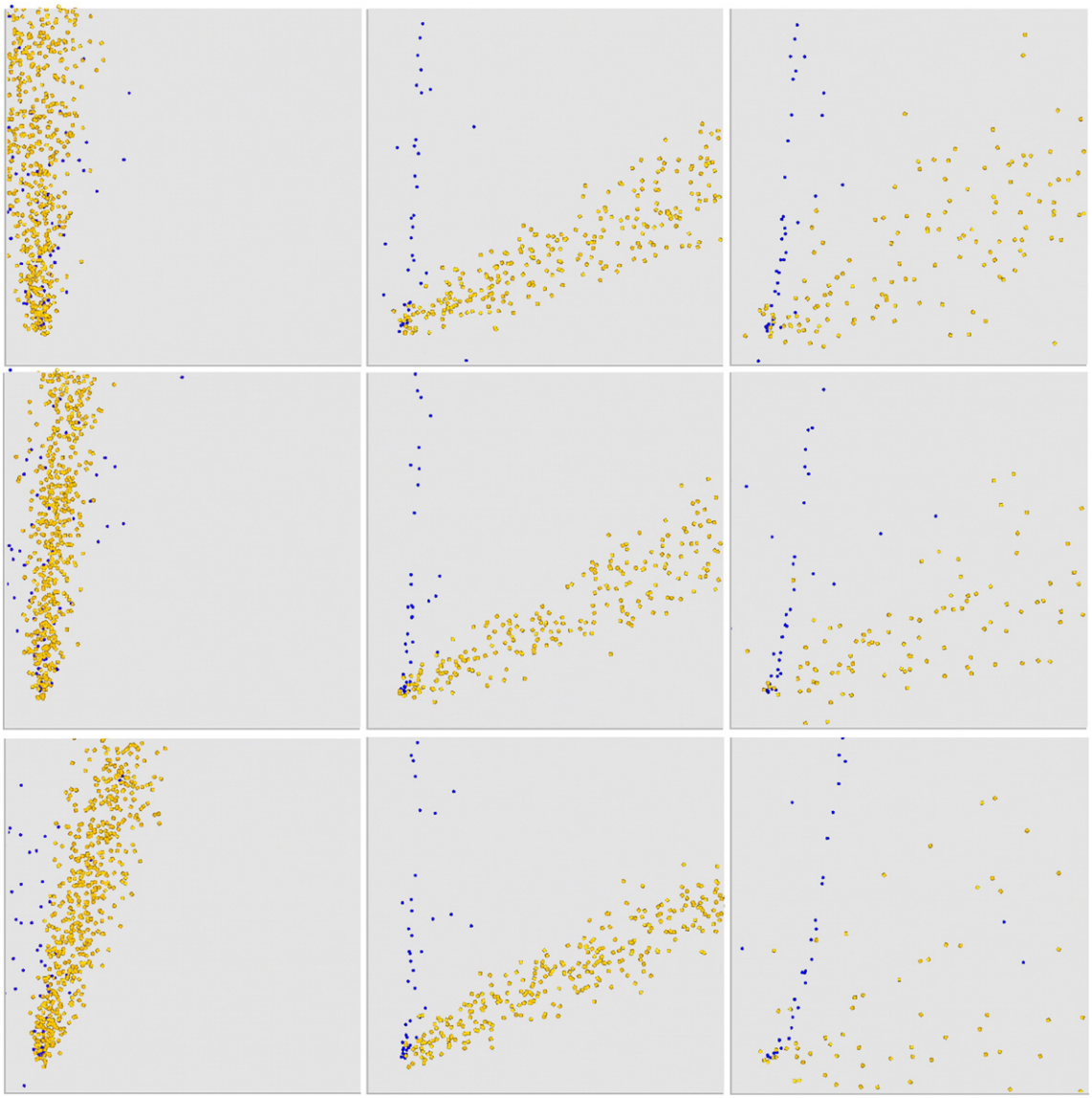

Fig. 15. Snapshots of the spherical particles (blue) and non-spherical particles (yellow) on the IVP, of which the amplitudes in two directions (x- and z-direction), A_x and A_z, are same, are 1, 3 and 5 mm, respectively (from top to bottom), and the vibration frequencies, f, meet the relation $A\cdot(2\pi f)^2 = 0.5g$, $A\cdot(2\pi f)^2 = 1.5g$ and $A\cdot(2\pi f)^2 = 2g$, respectively (from left to right). The other operating conditions are: $\beta = 2°$, $f_s = 0.6$, $e = 0.3$, $s_1 = s_2 = 5$, and $q = 30$ grains/s. Note that the snapshots are drawn when the separation of the mixtures reaches quasi-steady state, and the size of particles shown in the figure are ten times bigger than the real ones to ensure that they can be easily seen.

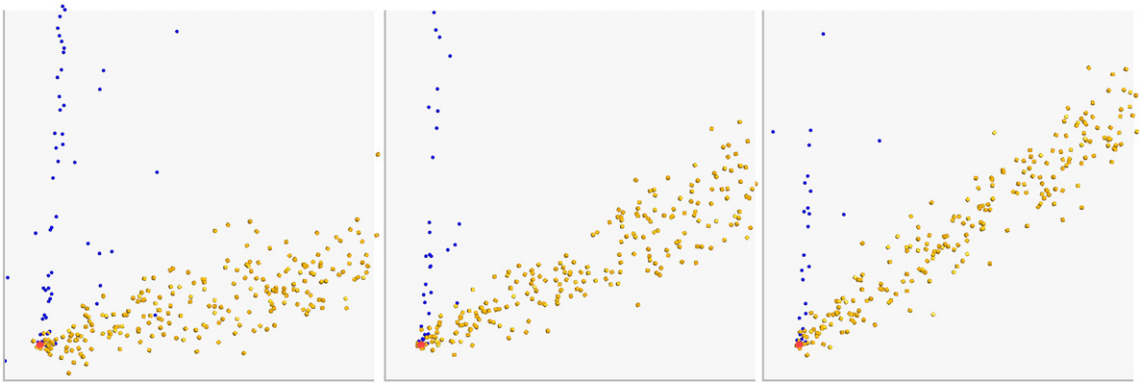

Fig. 16. Snapshots of the spherical particles (blue) and non-spherical particles (yellow) on the IVP with different inclination angle, β: 1°, 2°, and 3°, respectively (from left to right). The other operating conditions are: $A_x = A_z = 3$ mm, $f = 10$ Hz, $f_s = 0.6$, $e = 0.3$, $s_1 = s_2 = 5$, and $q = 30$ grains/s. Note that the snapshots are drawn when the separation of the mixtures reaches quasi-steady state, and the size of particles shown in the figure are ten times bigger than the real ones to ensure that they can be easily seen.

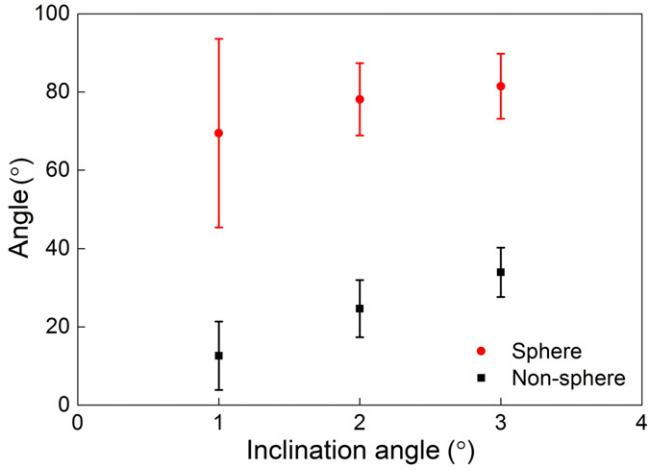

Fig. 17. Effect of the inclination angle of the IVP on particle separation. The other operating conditions are: $A_x = A_z = 3$ mm, $f = 10$ Hz, $f_s = 0.6$, $e = 0.3$, $s_1 = s_2 = 5$, and $q = 30$ grains/s.

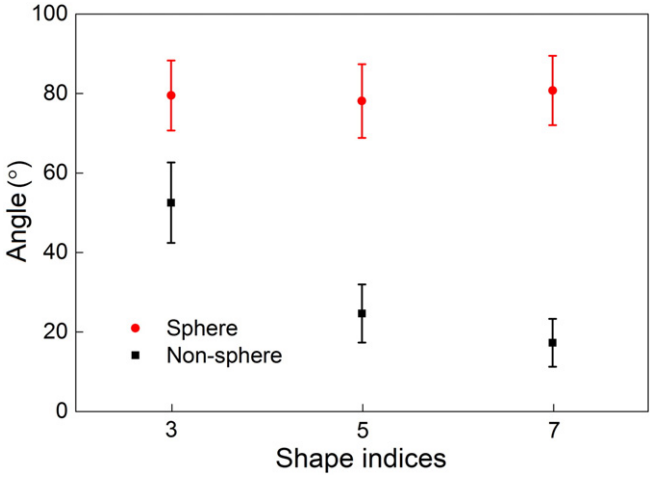

Fig. 19. Effect of the sphericity of non-sphericals on particle separation. The other operating conditions are: $\beta = 2°$, $A_x = A_z = 3$ mm, $f = 10$ Hz, $f_s = 0.6$, $e = 0.3$, and $q = 30$ grains/s.

where A and f are the vibration amplitude and vibration frequency of the IVP.

It is determined that the particle could take off from the IVP when the maximum vibration acceleration of the plate is more than the gravitational acceleration of the particle, and from Figs. 10 and 14 it can be seen that the phenomenon of the particle taking off from the IVP mainly occurs in the process of the IVP and particle moving upward. Thus, the vibration condition for the particle to take off can be written as:

$$A \cdot (2\pi f)^2 > g, \tag{28}$$

where $\boldsymbol{g}$ is the gravitational acceleration of the particle. When the vibration amplitude and frequency meet the equation $A \cdot (2\pi f)^2 = g$, we can get the critical vibration amplitude and frequency.

According to the Eq. (28), we did a series of simulation cases to investigate the effect of vibration amplitude and frequency variation on separation, and from the large number of simulation results we obtained that when the vibration amplitude and frequency meet the condition that $A \cdot (2\pi f)^2 \approx 1.5g$, the non-spherical particles can be separated from the spherical particles effectively. When the vibration amplitude and frequency do not satisfy the Eq. (28) such as $A \cdot (2\pi f)^2 = 0.5g$, the non-spherical particles cannot be separated from the spherical particles. Also, when the vibration amplitude and frequency meet the condition that $A \cdot (2\pi f)^2 > 1.5g$ such as $A \cdot (2\pi f)^2 = 2g$, the separation effect of particles significantly becomes bad. The corresponding simulation results of the above are shown in Fig. 15. In all other simulations, the amplitude and frequency meet the above variation rules and the results are not presented here for brevity.

According to the simulation results, we also found that the particle flight time greatly affect the separation of particles. By calculating the flight time of particles under different separation effects, we obtained that when the ratio of fly time of particles closes to 0.5, the separation effect is optimal because the particles can keep moving forward whether the plate moves forward or backward.

5.2. Effect of the inclination angle of the IVP

Apart from the vibration amplitude and frequency of the IVP mentioned above, the inclination angle of the IVP, β, is also one of the important operation parameters for particle separation. In this study, the inclination angle β is varied from 1° to 3°, and the corresponding snapshots of the particles on the IVP are shown in Fig. 16. Fig. 17 shows the quantitative results of the effect of the inclination angle of the IVP on particle separation. From these figures it can be seen clearly that the average angles of the two types of particles consistently increase with the increase of the inclination angle, while the dispersion degree of both species decreases. The reason is that the effect of gravity on the particles is increasing with the increase of the inclination angle of the IVP. When the inclination angle β is small, such as 1°, the effect of gravity is weak and the effect of friction is greater than that of gravity,

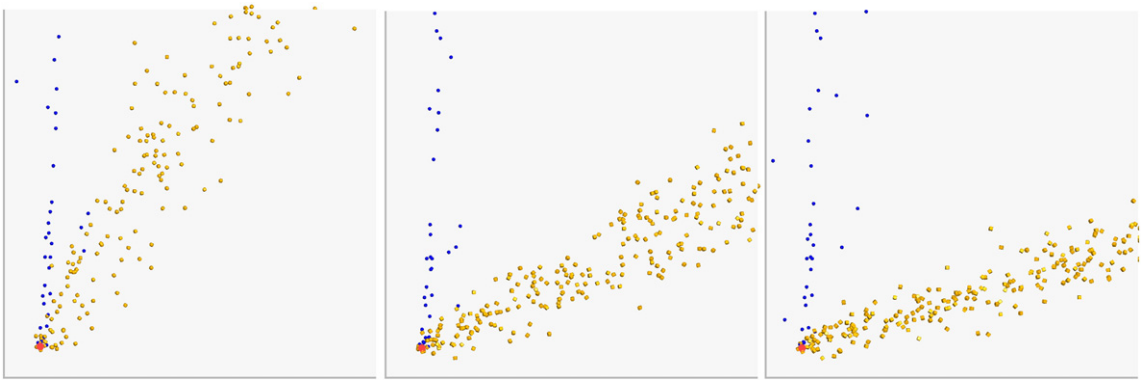

Fig. 18. Snapshots of the spherical particles (blue) and non-spherical particles (yellow) with different sphericity on the IVP, on which the shape indices of the on-spherical particles, s_1 and s_2, are 3, 5, and 7, respectively (from left to right). The other operating conditions are: $\beta = 2°$, $A_x = A_z = 3$ mm, $f = 10$ Hz, $f_s = 0.6$, $e = 0.3$, and $q = 30$ grains/s. Note that the snapshots are drawn when the separation of the mixtures reaches quasi-steady state, and the size of particles shown in the figure are ten times bigger than the real ones to ensure that they can be easily seen.

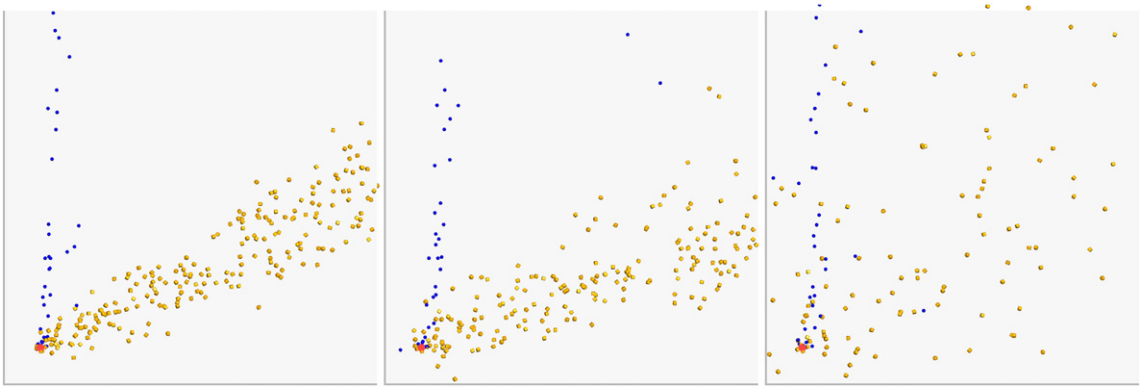

Fig. 20. Snapshots of the spherical particles (blue) and non-spherical particles (yellow) on the IVP, on which the restitution coefficients between particles and the IVP, e, are 0.3, 0.6, and 0.9, respectively (from left to right). The other operating conditions are: $\beta = 2°$, $A_x = A_z = 3$ mm, $f = 10$ Hz, $f_s = 0.6$, $s_1 = s_2 = 5$, and $q = 30$ grains/s. Note that the snapshots are drawn when the separation of the mixtures reaches quasi-steady state, and the size of particles shown in the figure are ten times bigger than the real ones to ensure that they can be easily seen.

which causes the particles to move slowly and accumulate on the plate, so both spherical particles and non-spherical particles are relatively dispersed. With the increase of the inclination angle, the effect of gravity is enhanced and that of the friction has almost no increase. For non-spherical particles in the simulation case with the inclination angle of 3°, the average angle increases from about 12° to about 34° comparing to that as $\beta = 1°$; for spherical particles, the average angle increases from about 69° to about 81°, while the separation angle between the spherical particles and non-spherical particles has no change. Then it can be obtained that changing the inclination angle of the IVP has certain influence on the movement direction of each kind of particles, whereas the impact on the separation effect of the mixed particles is small.

5.3. Effect of the particle properties

In addition to the operating parameters of the IVP, the movement behavior of particles on the IVP also depends on the shape and mechanical properties of particles. Note that in the following discussions, the inclination angle of the plate is set to a fixed value (2°) that no longer change throughout the following simulation cases. In this study, the particles are described by super-ellipsoids, which have two shape indices s_1 and s_2, and the particles are spherical when $s_1 = s_2 = 2$. The non-spherical particles with different sphericities can be simulated by super-ellipsoids when s_1 and s_2 are larger than 2. Here, we use $s_1 = s_2 = 3$, $s_1 = s_2 = 5$, and $s_1 = s_2 = 7$ to investigate the effect of the sphericity of particle on separation efficiency and the shape of particles is shown in Fig. 1. The corresponding snapshots of the particles with different sphericities are shown in Fig. 18. It can be found that the separation efficiency of the mixtures is greatly enhanced with the decrease of the sphericity of particles (*i.e.* the increase of s_1 and s_2), which indicates that particle shape plays a very significant role in the separation of the mixtures. Fig. 19 shows that the average separation angle between the two species significantly increases from about 27° to about 63° with the shape indices increase from 3 to 7 while the dispersion degree of the two species is relatively small and almost have no change with the variation of the shape indices. The reason is that the friction force between non-spherical particles and the plate (*i.e.* the driving force of non-spherical particles) is greater than that of spherical particles, and the smaller the sphericity of non-spherical particles, the larger driving force of non-spherical particles when they sliding on the IVP. The motion of non-spherical particles is weakened in the y-direction while that is enhanced in the x-direction due to the large frictional resistance. So when the sphericity of non-spherical particles is small, the non-spherical particles can be more effectively separated from the spherical particles.

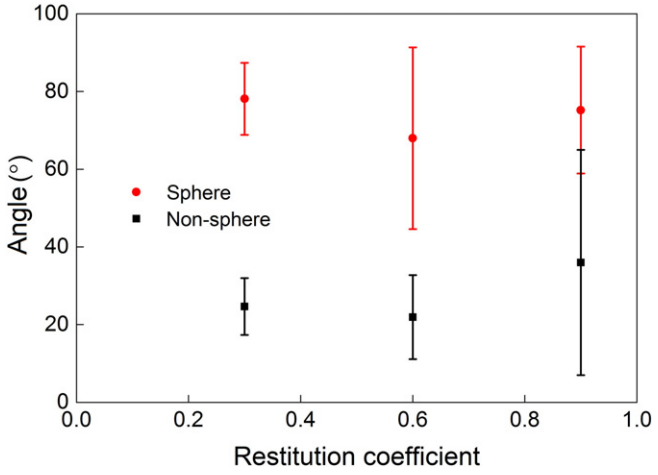

Fig. 21. Effect of the restitution coefficient between particles and the IVP on particle separation. The other operating conditions are: $\beta = 2°$, $A_x = A_z = 3$ mm, $f = 10$ Hz, $f_s = 0.6$, $s_1 = s_2 = 5$, and $q = 30$ grains/s.

5.4. Effect of the restitution coefficient

In order to select appropriate material used for the vibrating plate to enhance the separation efficiency of the mixtures, the collision parameters between particles and the plate such as the restitution coefficient need to be investigated. Fig. 20 shows the snapshots of the spherical particles and non-spherical particles on the IVP with different restitution coefficients. It can be seen that the separation effect of the mixtures is good when the restitution coefficient is small such as 0.3, but the two species particles are completely inseparable when the restitution coefficient increases to 0.9. Fig. 21 shows the quantitative results of the effect of the restitution coefficient on particle separation. When the restitution coefficient gradually increases from 0.3 to 0.9, the average separation angle between the two species decreases from about 53° to about 39° and the dispersion degree of the two species increases obviously.

The effect of restitution coefficient on separation can be explained by tracking the trajectory of a particle motion on the IVP, and Fig. 22 shows the z-direction displacement-time curves of a non-spherical particle and the IVP. From this figure we can see that when the restitution coefficient is small, the particle keeps touching with the IVP when the plate moves forward and then bounces from the plate when the IVP moves back, so the particle can move forward with high transport velocity in the entire separation cycle, just like that shown in Fig. 11b. When the restitution coefficient is too large (0.9 here), the particle

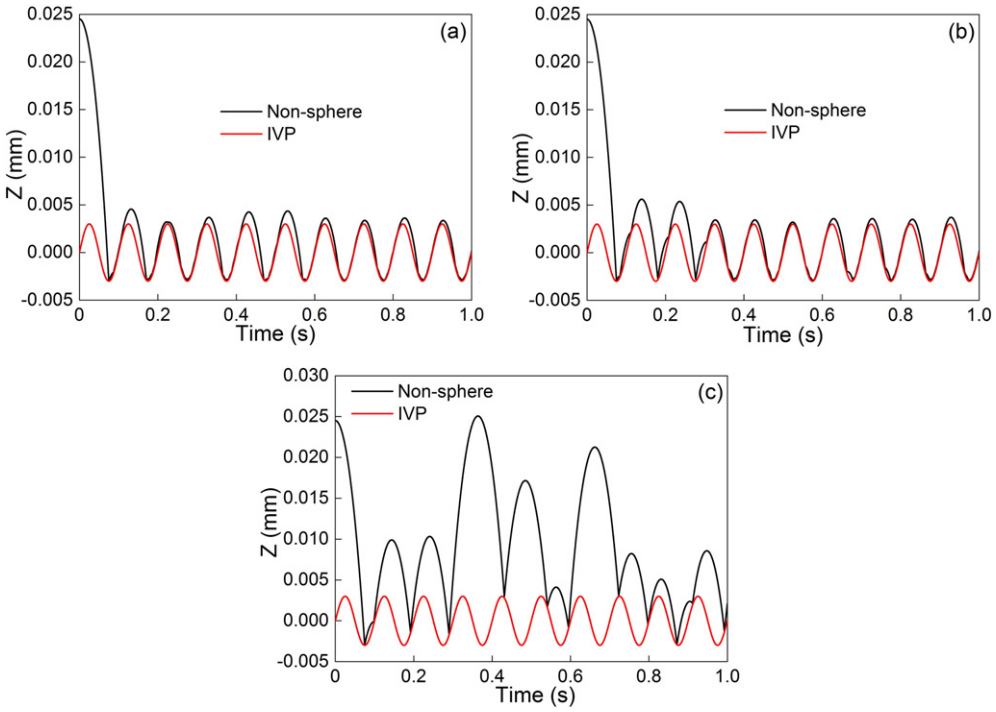

Fig. 22. The *z*-direction displacement-time curves of the non-spherical particle and the IVP: (a) $e = 0.3$, (b) $e = 0.6$, (c) $e = 0.9$. The other operating conditions are: $\beta = 2°$, $A_x = A_z = 3$ mm, $f = 10$ Hz, $f_s = 0.6$, $s_1 = s_2 = 5$, $e = 0.3$, and $q = 30$ grains/s.

almost only keeps jumping on the IVP so the residence time of the particle on the plate significantly reduces and the particle cannot be transported regularly on the IVP under the effect of IVP vibration. This is the reason why the dispersion degree of particles increases significantly, as shown in Fig. 20. Then it can be found that the vibrating plate with too large restitution coefficient has no positive effect on improving the separation effect of the mixtures, and the selection of the material for the vibrating plate should be reasonable.

5.5. Effect of the friction coefficient

In addition to the restitution coefficient, the friction coefficient is another important collision parameter between particles and the plane. Here, four different friction coefficients, 0.2, 0.4, 0.6, and 0.8 were used to explore the effect of the friction coefficient on particle separation. In this study, the rolling friction coefficient is ignored because it nearly has no effect on particles separation. The snapshots of the spherical particles and non-spherical particles on the IVP with different friction coefficients are shown in Fig. 23, and the quantitative results of the effect of the friction coefficient on particle separation are shown in Fig. 24. From these figures it can be seen that the friction coefficient has little influence on the separation of the mixtures. The reason is that, in the present simulations, the main influence factors of particle segregation such as the vibration amplitude, vibration frequency and the inclination angle of the IVP have been set in an appropriate range, and even the small friction coefficient like 0.2 can produce enough driving force for non-spherical particles. Thus, the friction coefficient in the normal range (from 0.2 to 0.8) nearly has no effect on particle separation on the IVP.

5.6. Effect of the feed rate of particles

Besides the vibration of the IVP and other properties of the collision system, the feed rate of particles is another factor need to be considered because it determines the handling capacity of the IVP. Here, five feed rates, 10, 20, 30, 40, and 50 grains/s were adopted in the simulations. Fig. 25 shows the snapshots of the spherical particles and non-spherical particles on the IVP under different feed rates, and the quantitative results of the effect of the feed rate of particles on particle separation are shown in Fig. 26. From these figures it can be seen that the

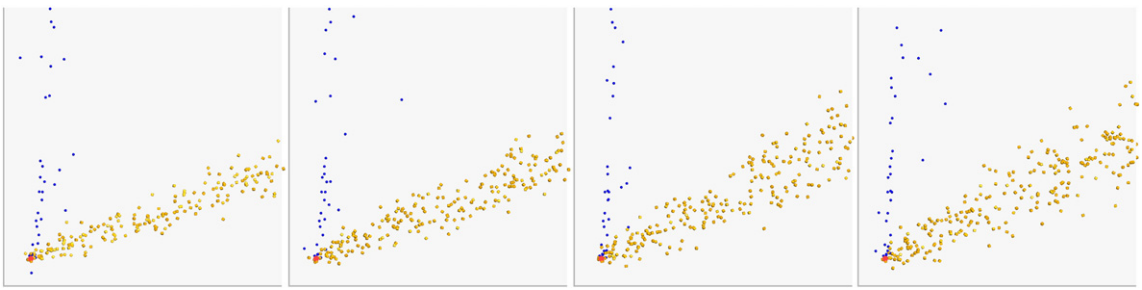

Fig. 23. Snapshots of the spherical particles (blue) and non-spherical particles (yellow) on the IVP, on which the friction coefficients between particles and the IVP, f_s, are 0.2, 0.4, 0.6, and 0.8, respectively (from left to right). The other operating conditions are: $\beta = 2°$, $A_x = A_z = 3$ mm, $f = 10$ Hz, $s_1 = s_2 = 5$, $e = 0.3$, and $q = 30$ grains/s. Note that the snapshots are drawn when the separation of the mixtures reaches quasi-steady state, and the size of particles shown in the figure are ten times bigger than the real ones to ensure that they can be easily seen.

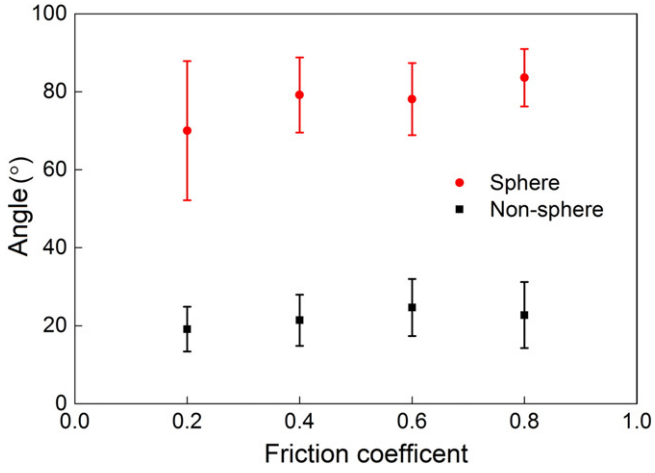

Fig. 24. Effect of the friction coefficient between particles and the IVP on particle separation. The other operating conditions are: $\beta = 2°$, $A_x = A_z = 3$ mm, $f = 10$ Hz, $f_s = 0.6$, $s_1 = s_2 = 5$, and $q = 30$ grains/s.

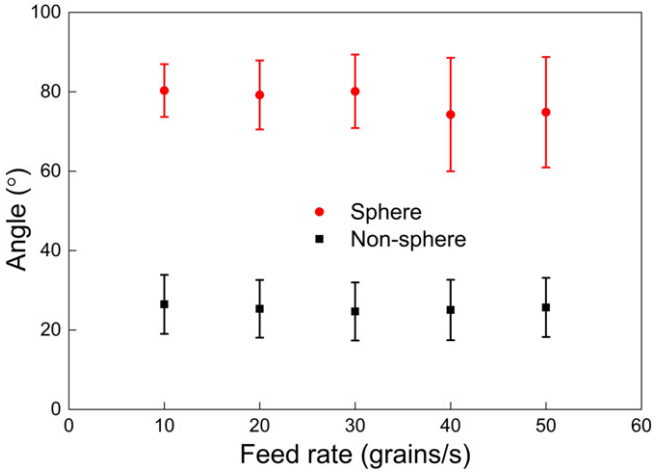

Fig. 26. Effect of the feed rate of particles on particle separation. The other operating conditions are: $\beta = 2°$, $A_x = A_z = 3$ mm, $f = 10$ Hz, $f_s = 0.6$, $s_1 = s_2 = 5$, and $e = 0.3$.

average angles of both spherical particles and non-spherical particles change little with the increase of feed rate, while the number of particles on the IVP increases significantly, and the dispersion degree of spherical particles are larger than that of non-spherical particles. The reason is as follows: when the feed rate of the mixed particles is low, there is no interaction between particles due to the small number of particles, which makes spherical particles roll uniformly in the y-direction. But with the increase of feed rate of particles, the number of particles increases then the interaction between particles is obvious, causing the particles to collide with each other when they moving on the IVP, so the dispersion degree of the spherical particles increases significantly. In this research, the effect of the feed rate on particle separation is not obvious because the feed rates of particles adopted in this study are not high.

5.7. Effect of the particle size

To investigate the effect of particle size on separation, we also adopted bigger particles with the half-lengths of 1 mm, 2 mm and 5 mm. A series of simulations were done and from the simulation results we can obtained that the vibration amplitude and frequency of plate should be adjusted correspondingly with the increase of particle size. However, whether the particle size increases or decreases, the change of the inclination angle of plate, feed rates of particles or other governing parameters has little effect on the separation of the mixtures. When the vibration amplitude and frequency of the plate meet the Eq. (28), there are an optimal vibration amplitude and frequency, which can be expressed as A_0 and f_0, respectively. When the size of the particle enlarges N times, the vibration amplitude accordingly needs to be expanded N times to achieve the similar separation effect. Then the relationship can be written as:

$$A_n = NA_0, \tag{29}$$

where A_n is the corresponding vibration amplitude of the plate when the particle size is enlarged N times. And according to Eqs. (28) and (29), the corresponding vibration frequency can be written as:

$$f_n^2 = f_0^2/N, \tag{30}$$

where f_n is the corresponding vibration frequency of the plate when the particle size is enlarged N times.

6. Conclusions

The effect of various operating conditions on separating non-spherical particles from spherical particles on the IVP was investigated by the DEM simulation based on super-ellipsoids. From the results obtained, the following conclusions can be drawn:

(1) The vibration amplitude and frequency of the IVP have great impact on particle separation, and when the vibration amplitude and frequency meet the condition $A \cdot (2\pi f)^2 \approx 1.5g$, the optimal separation effect of particles can be obtained in this research. Besides, when the particle size enlarges N times, the adjusted optimal amplitude and frequency should meet the equation $A_n = NA_0$ and $f_n^2 = f_0^2/N$, respectively. Comparing with the vibration of IVP, the inclination angle of the IVP has no obvious influence on particle separation when the angle increases from 1° to 3°.

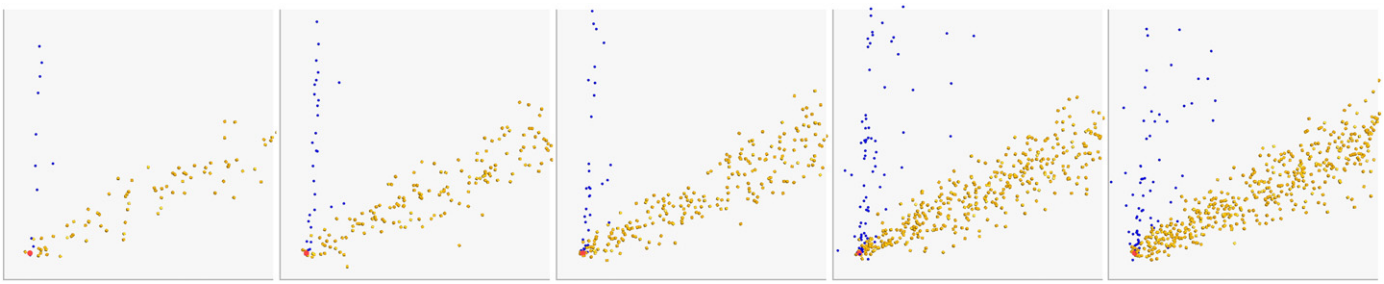

Fig. 25. Snapshots of the spherical particles (blue) and non-spherical particles (yellow) on the IVP, on which the particles are fed with different rate, q, are 10, 20, 30, 40, and 50 grains/s, respectively (from left to right). The other operating conditions are: $\beta = 2°$, $A_x = A_z = 3$ mm, $f = 10$ Hz, $f_s = 0.6$, $s_1 = s_2 = 5$, and $e = 0.3$. Note that the snapshots are drawn when the separation of the mixtures reaches quasi-steady state, and the size of particles shown in the figure are ten times bigger than the real ones to ensure that they can be easily seen.

(2) The separation behavior of spherical particles and non-spherical particles also depends on the properties of the particles, such as the particle shape. When the sphericity of the non-spherical particles is small, the non-spherical particles can be more effectively separated from the spherical particles.
(3) The collision parameters between particles and the plate such as the restitution coefficient are important for particle separation. It can be found that the smaller the restitution coefficient is, the better the separation effect is. Thus, we need to select appropriate material used for the vibrating plate to enhance the separation efficiency of the mixtures. But the change of friction coefficient in the normal range (from 0.2 to 0.8) has little effect on particle separation.
(4) When other parameters are determined, changing the feed rate of particles has little effect on the separation effect of the mixtures. But the number of particles on the IVP increases significantly with the feed rate of particles increases, and the dispersion degree of the two species particles slightly increases.

Acknowledgments

This research is financially supported by the National Natural Science Foundation of China (NSFC, Grant No. 21476193).

References

[1] M. Sugimoto, K. Yamamoto, J.C. Williams, Continuous separation of spherical and non-spherical particles on an inclined rotating disc, J. Chem. Eng. Jpn. 10 (1977) 137–141.
[2] K. Viswanathan, S. Aravamudhan, B.P. Mani, Separation based on shape part I: recovery efficiency of spherical particles, Powder Technol. 39 (1984) 83–91.
[3] F.G. Carpenter, V.R. Deitz, Glass spheres for the measurement of the effective opening of testing sieves, J. Res. Natl. Bur. Stand. 47 (1951) 139.
[4] K. Yamamoto, M. Makino, M. Sugimoto, Investigation of the shape separation performance of a rotating conical disk based on the rolling frictional characteristics of irregular particles, J. Res. Assoc. Powder Technol. Jpn. 29 (1992) 669–675.
[5] K. Yamamoto, Y. Tamao, M. Sugimoto, The separation of irregular-shaped fine particles using a rotating vibrating conical disk, J. Res. Assoc. Powder Technol. Jpn. 32 (1995) 612–616.
[6] K. Yamamoto, M. Tohyama, M. Sugimoto, Continuous separation of differently shaped fine particles on a rotating vibrating conical disk-effects of different operating conditions on separation characteristics under various throughputs, Powder Technol. 99 (1998) 1–10.
[7] K. Yamamoto, T. Okumura, M. Sugimoto, The separation of irregularly shaped fine particles by a vibrating rotating disk, Adv. Powder Technol. 9 (1998) 81–95.
[8] M. Furuuchi, K. Gotoh, Shape separation of particles, Powder Technol. 73 (1992) 1–9.
[9] K. Yamamoto, T. Tsukada, M. Sugimoto, A consideration of the mechanism of particle shape separation by a rotating conical disk with a spiral scraper, J. Res. Assoc. Powder Technol. Jpn. 26 (1989) 12–22.
[10] B. Waldie, Separation of particles according to shape, Powder Technol. 7 (1973) 244–246.
[11] M. Nakagawa, M. Furuuchi, M. Yamahata, K. Gotoh, J.K. Beddow, Shape classification of granular materials by rotating cylinder with blades, Powder Technol. 44 (1985) 195–202.
[12] M. Furuuchi, K. Gotoh, Continuous shape separation of binary mixture of granular particles, Powder Technol. 54 (1988) 31–37.
[13] K. Ridgway, R. Rupp, A. Sanchez, The mixing of powders flowing down an inclined plane, J. Pharm. Pharmacol. 20 (1968) 185–193.
[14] E. Abe, H. Hirosue, Continuous separation of particles according to shape on an inclined vibrating plate, J. Chem. Eng. Jpn. 15 (1982) 323–326.
[15] S. Endoh, Sorting of particles by inclined vibrating plate I. Analysis of the motion of particles on an inclined vibrating plate, Powder Technol. 50 (1987) 103–109.
[16] S. Koyanaka, H. Ohya, S. Endoh, H. Iwata, P. Ditl, Recovering copper from electric cable wastes using a particle shape separation technique, Adv. Powder Technol. 8 (1997) 103–111.
[17] Z. Rchez, Devices for dry separation of the spherical particles from those having a non-spherical shape from a metallic powder, Adv. Mater. Res. 23 (2007) 91–94.
[18] B. Yang, Y.L. Shao, J.G. Zhu, B.Z. Zhang, L.F. Sun, Q.J. Lu, K.Y. Zhang, Shape sorting of coated fuel particles, Atom. Energ. Sci. Technol. 37 (2003) 53–55.
[19] P.A. Cundall, O.D.L. Strack, A discrete numerical mode for granular assemblies, Geotechnique 29 (1979) 47–65.
[20] H. Zhu, Z. Zhou, R. Yang, A. Yu, Discrete particle simulation of particulate systems: a review of major applications and findings, Chem. Eng. Sci. 63 (2008) 5728–5770.
[21] J.F. Favier, M.H. Abbaspour-Fard, M. Kremmer, A.O. Raji, Shape representation of axi-symmetrical, non-spherical particles in discrete element simulation using multi-element model particles, Eng. Comput. 16 (1999) 467–480.
[22] H. Kruggel-Emden, S. Rickelt, S. Wirtz, V. Scherer, A study on the validity of the multi-sphere discrete element method, Powder Technol. 188 (2008) 153–165.
[23] M.H. Abbaspour-Fard, Theoretical validation of a multi-sphere, discrete element model suitable for biomaterials handling simulation, Biosyst. Eng. 88 (2004) 153–161.
[24] M. Kodam, R. Bharadwaj, J. Curtis, B. Hancock, C. Wassgren, Force model considerations for glued-sphere discrete element method simulations, Chem. Eng. Sci. 64 (2009) 3466–3475.
[25] M. Kodam, J. Curtis, B. Hancock, C. Wassgren, Discrete element method modeling of bi-convex pharmaceutical tablets: contact detection algorithms and validation, Chem. Eng. Sci. 69 (2012) 587–601.
[26] M.M.M. Shamsi, A.A. Mirghasemi, Numerical simulation of 3D semi-real-shaped granular particle assembly, Powder Technol. 221 (2012) 431–446.
[27] E.G. Nezami, Y.M.A. Hashash, D. Zhao, J. Ghaboussi, A fast contact detection algorithm for 3-D discrete element method, Comput. Geotech. 31 (2004) 575–587.
[28] A. Wachs, L. Girolami, G. Vinay, G. Ferrer, Grains3D, a flexible DEM approach for particles of arbitrary convex shape-part I: numerical model and validations, Powder Technol. 224 (2012) 374–389.
[29] J.M. Ting, B.T. Corkum, Computational laboratory for discrete element geomechanics, J. Comput. Civ. Eng. 6 (1992) 129–146.
[30] J.M. Ting, A robust algorithm for ellipse-based discrete element modelling of granular materials, Comput. Geotech. 13 (1992) 175–186.
[31] H. Ouadfel, L. Rothenburg, An algorithm for detecting inter-ellipsoid contacts, Comput. Geotech. 24 (1999) 245–263.
[32] A. Džiugys, B. Peters, A new approach to detect the contact of two-dimensional elliptical particles, Int. J. Numer. Anal. Methods Geomech. 25 (2001) 1487–1500.
[33] Z.Y. Zhou, D. Pinson, R.P. Zou, A.B. Yu, Discrete particle simulation of gas fluidization of ellipsoidal particles, Chem. Eng. Sci. 66 (2011) 6128–6145.
[34] W. Xu, H. Chen, Mesostructural characterization of particulate composites via a contact detection algorithm of ellipsoidal particles, Powder Technol. 221 (2012) 296–305.
[35] R.M. Baram, P.G. Lind, Deposition of general ellipsoidal particles, Phys. Rev. E 85 (2012) 041301.
[36] M. Kodam, R. Bharadwaj, J. Curtis, B. Hancock, C. Wassgren, Cylindrical object contact detection for use in discrete element method simulations. Part I-contact detection algorithms, Chem. Eng. Sci. 65 (2010) 5852–5862.
[37] M. Kodam, R. Bharadwaj, J. Curtis, B. Hancock, C. Wassgren, Cylindrical object contact detection for use in discrete element method simulations, part II-experimental validation, Chem. Eng. Sci. 65 (2010) 5863–5871.
[38] Y. Guo, C. Wassgren, W. Ketterhagen, B. Hancock, J. Curtis, Some computational considerations associated with discrete element modeling of cylindrical particles, Powder Technol. 228 (2012) 193–198.
[39] J. Li, P.A. Langston, C. Webb, T. Dyakowski, Flow of sphero-disc particles in rectangular hoppers-a DEM and experimental comparison in 3D, Chem. Eng. Sci. 59 (2004) 5917–5929.
[40] Y. Song, R. Turton, F. Kayihan, Contact detection algorithms for DEM simulations of tablet-shaped particles, Powder Technol. 161 (2006) 32–40.
[41] F.Y. Fraige, P.A. Langston, G.Z. Chen, Distinct element modelling of cubic particle packing and flow, Adv. Powder Technol. 186 (2008) 224–240.
[42] M. Yao, A. Anandarajah, Three-dimensional discrete element method of analysis of clays, J. Eng. Mech. 129 (2003) 585–596.
[43] G. Lu, J.R. Third, C.R. Müller, Discrete element models for non-spherical particle systems: from theoretical developments to applications, Chem. Eng. Sci. 127 (2015) 425–465.
[44] J.R. Williams, A.P. Pentland, Superquadrics and modal dynamics for discrete elements in interactive design, Eng. Comput. 9 (1992) 115–127.
[45] C. Wellmann, C. Lillie, P. Wriggers, Homogenization of granular material modeled by a three-dimensional discrete element method, Comput. Geotech. 35 (2008) 394–405.
[46] P.W. Cleary, Large scale industrial DEM modelling, Eng. Comput. 21 (2004) 169–204.
[47] Y. Jiao, F.H. Stillinger, S. Torquato, Distinctive features arising in maximally random jammed packings of superballs, Phys. Rev. E 81 (2010) 041304.
[48] G. Lu, J. Third, C. Müller, Critical assessment of two approaches for evaluating contacts between super-quadric shaped particles in DEM simulations, Chem. Eng. Sci. 78 (2012) 226–235.
[49] K. Kiangi, A. Potapov, M. Moys, DEM validation of media shape effects on the load behaviour and power in a dry pilot mill, Miner. Eng. 46 (2013) 52–59.
[50] D. Höhner, S. Wirtz, V. Scherer, A study on the influence of particle shape on the mechanical interactions of granular media in a hopper using the discrete element method, Powder Technol. 278 (2015) 286–305.
[51] A.H. Barr, Superquadrics and angle-preserving transformations, IEEE Comput. Graph. Appl. 1 (1981) 11–23.
[52] Y. Zhao, M. Jiang, Y. Liu, J. Zheng, Particle-scale simulation of the flow and heat transfer behaviors in fluidized bed with immersed tube, AICHE J. 55 (2009) 3109–3124.
[53] Y. Zhao, Y. Cheng, C. Wu, Y. Ding, Y. Jin, Eulerian-Lagrangian simulation of distinct clustering phenomena and RTDs in riser and downer, Particuology 8 (2010) 44–50.
[54] M. Jiang, Y. Zhao, G. Liu, J. Zheng, Enhancing mixing of particles by baffles in a rotating drum mixer, Particuology 9 (2011) 270–278.
[55] Y. Zhao, L. Xu, J. Zheng, CFD-DEM simulation of tube erosion in a fluidized bed, AICHE J. 63 (2017) 418–437.